

Localization of protoporphyrin IX during glioma-resection surgery via paired stimulated Raman histology and fluorescence microscopy

Received: 3 April 2022

Accepted: 20 April 2024

Published online: 10 July 2024

 Check for updates

A list of authors and their affiliations appears at the end of the paper

The most widely used fluorophore in glioma-resection surgery, 5-aminolevulinic acid (5-ALA), is thought to cause the selective accumulation of fluorescent protoporphyrin IX (PpIX) in tumour cells. Here we show that the clinical detection of PpIX can be improved via a microscope that performs paired stimulated Raman histology and two-photon excitation fluorescence microscopy (TPEF). We validated the technique in fresh tumour specimens from 115 patients with high-grade gliomas across four medical institutions. We found a weak negative correlation between tissue cellularity and the fluorescence intensity of PpIX across all imaged specimens. Semi-supervised clustering of the TPEF images revealed five distinct patterns of PpIX fluorescence, and spatial transcriptomic analyses of the imaged tissue showed that myeloid cells predominate in areas where PpIX accumulates in the intracellular space. Further analysis of external spatially resolved metabolomics, transcriptomics and RNA-sequencing datasets from glioblastoma specimens confirmed that myeloid cells preferentially accumulate and metabolize PpIX. Our findings question 5-ALA-induced fluorescence in glioma cells and show how 5-ALA and TPEF imaging can provide a window into the immune microenvironment of gliomas.

The optimal surgical care of patients with glioma requires a careful balance between maximal tumour resection and the preservation of neurologic function. Fluorescence guidance with 5-aminolevulinic acid (5-ALA) is one of the most well-studied and evidence-supported approaches for maximizing extent of resection in patients with high-grade glioma (HGG)^{1–3}. The use of 5-ALA increases the chances for radiographically complete tumour resection, the clinical gold standard in glioma surgery, by 63–89% (refs. 1,3–7).

The best published evidence in patients with glioblastoma (GBM) suggests that 5-ALA-induced fluorescence is most intense in densely tumour-infiltrated tissue and decreases towards the tumour periphery^{8,9}. Unfortunately, widely employed techniques for visualization of

5-ALA-induced fluorescence are limited by poor sensitivity, particularly at tumour margins¹⁰. Consequently, the negative predictive value of 5-ALA-induced fluorescence in HGG has been estimated to be as low as 21%^{1,7,11–16}.

Both cell-intrinsic factors such as altered haem metabolism and attributes of the brain tumour microenvironment are hypothesized to play a role in the 5-ALA-induced fluorescence in high-grade gliomas¹⁷. In vitro evidence suggests that 5-ALA causes fluorescence within glioma cells because of ferrochelatase dysfunction, which leads to intracellular accumulation of PpIX^{18–21}. Several clinical studies point to a key role for blood–brain barrier breakdown in determining which tumours will visibly fluoresce due to protoporphyrin IX (PpIX) accumulation^{22,23}.

✉ e-mail: dieter.henrik.heiland@uniklinik-freiburg.de; Daniel.Orringer@nyulangone.org

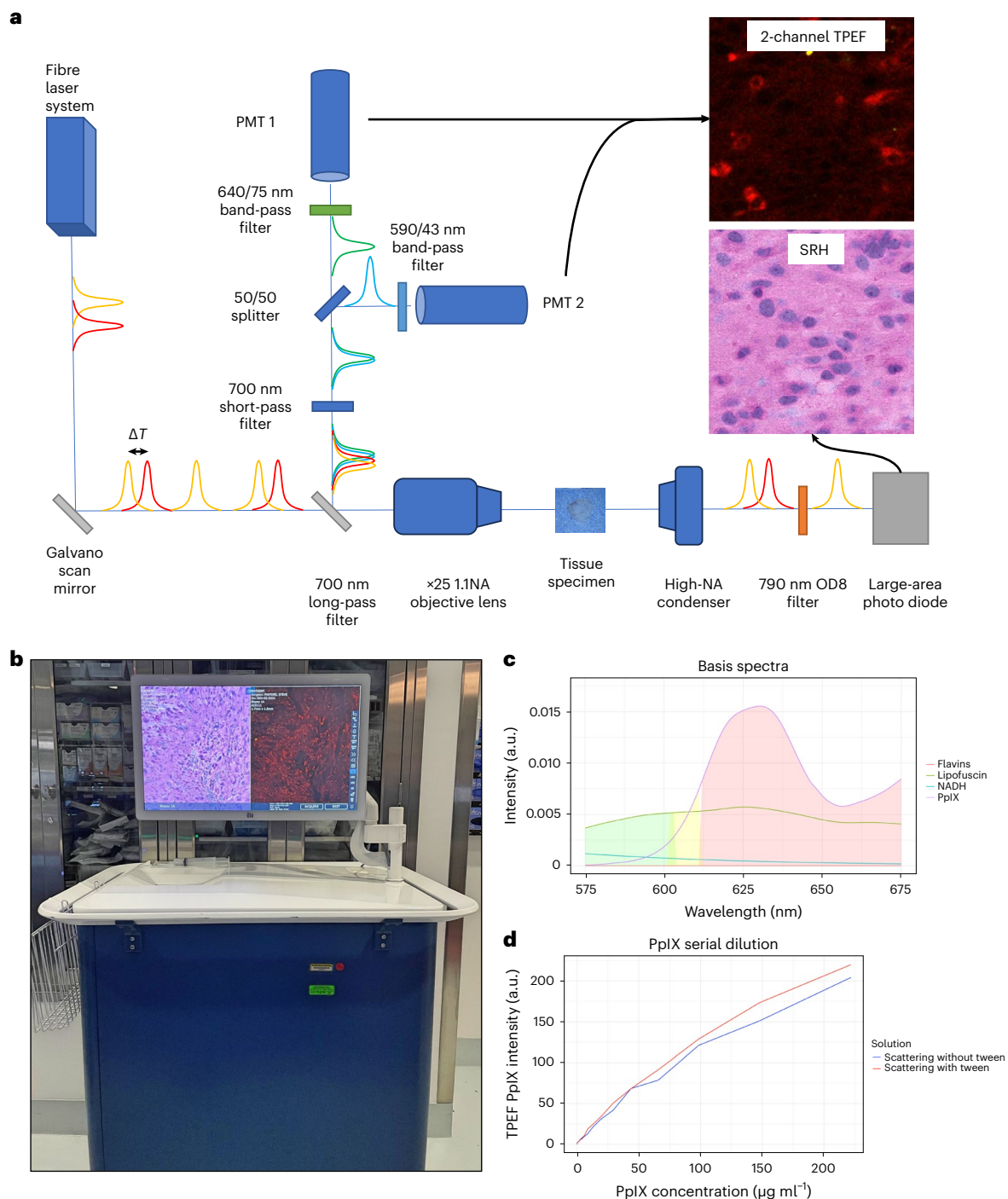


Fig. 1 | Engineering a paired SRH/TPEF microscope. Building on an existing fibre laser-based microscope developed for clinical stimulated Raman scattering microscopy, we developed a paired SRH/TPEF microscope. **a**, Excitation impulses (790 and 1,010–1,040 nm) are generated by a fibre laser and employed to induce both stimulated Raman scattering, collected in transmission via a photodiode, and TPEF, collected in reflection, filtered as shown and detected with two

high-sensitivity photomultiplier tubes. **b**, SRH and TPEF images are displayed with the same fields of view in a split-screen format. **c**, The ranges of emission detected by PMT₁ (602–677 nm, red), PMT₂ (568–611 nm, green) as well as their overlap (yellow) are shown on a graph depicting the emission spectra of PpIX and autofluorophors NADH, flavins and lipofuscin. **d**, Fluorescence intensity increases in a dose-dependent manner with increasing PpIX concentration.

Accordingly, fluorescence observed in patients with 5-ALA-treated glioma is hypothesized to reflect both intracellular PpIX accumulation within tumour cells and local blood–brain barrier breakdown.

Indeed, bright 5-ALA-induced fluorescence is highly predictive for the presence of tumour infiltration¹⁰. Brain tissue infiltrated by a higher concentration of tumour cells, especially in regions where there is blood–brain barrier breakdown, would therefore be hypothesized to fluoresce more strongly than brain tissue with a lesser degree of

tumour infiltration behind an intact blood–brain barrier. Low levels of 5-ALA-induced fluorescence at glioma margins and in tumours with mild to moderate cellularity are thought to occur because of the challenge of detecting increasingly sparse fluorescing tumour cells in which there is a low level of PpIX accumulation²⁴.

Intriguingly, 5-ALA-induced tumour cell fluorescence in 5-ALA-treated glioma tissue has not been well documented²⁵. Previously, we developed and validated a US Food and Drug Administration

(FDA)-registered clinical stimulated Raman histology (SRH) microscopy system to streamline the process for accessing histologic data in the operating room^{26–29}. SRH is achieved in the operating room through the use of an Er-Yb fibre laser that can also be utilized to induce two-photon fluorescence. We hypothesized that creating a bifunctional imaging system capable of performing both SRH and two-photon fluorescence (TPEF) microscopy at precisely the same spatial coordinates within tissue specimens would offer an unprecedented opportunity to directly visualize the microscopic localization of PpIX in human brain tumours. In addition, the utilization of two-photon microscopic techniques enables optical sectioning in fresh human specimens, minimizing the decay of PpIX signal that can be caused by photobleaching and chemical degradation.

Our study in 115 patients with high-grade glioma yielded several unexpected findings. We noted that tissue cellularity does not have a direct relationship with 5-ALA-induced fluorescence and that only a subset of imaged cells concentrated PpIX. Semi-supervised clustering of TPEF images demonstrated five different patterns of PpIX fluorescence. We conducted spatial transcriptomics on tissue imaged with the SRH/TPEF microscope, and we noted that PpIX accumulates most avidly in cells of myeloid origin, morphologically consistent with tumour-associated macrophages. We verified the observation that PpIX accumulation occurred in tumour-associated macrophages using external datasets of spatially resolved metabolomics and RNA sequencing. Our data therefore create the possibility of a tumour-cell-independent mechanism for PpIX accumulation in human brain tumours. This study also shows how innovations in optics can advance our understanding of the cellular biodistribution of clinical fluorophores and offer a novel means of imaging the tumour-immune milieu.

Results

Engineering a multimodal optical system for SRH and TPEF

We modified an existing, FDA-registered clinical system for stimulated Raman histology (Fig. 1a,b) by adding a two-channel epifluorescence module to allow simultaneous detection of SRH and PpIX fluorescence from the same optical section in fresh human brain tumour specimens. Stimulated Raman scattering (SRS) is excited with a custom dual-wavelength picosecond (2–3 ps) fibre laser source with a fixed wavelength pump beam at 790 nm and a Stokes beam tunable from 1,010 nm to 1,040 nm³⁰. SRS is detected in transmission mode with a large area photodiode (PD). As described previously²⁸, we combine high-frequency lock-in detection at 10 MHz with high-speed auto-balanced detection to achieve high detection sensitivity. We use a high-NA water-immersion objective lens (Olympus $\times 25/1.05\text{NA}$) to achieve high resolution in tissue specimens. For SRH, we image the sample sequentially at 2,845 cm^{-1} to detect primarily lipids and at 2,940 cm^{-1} to detect primary protein and DNA, and apply a pseudo-colour scheme that mimics traditional haematoxylin and eosin (H&E) staining²⁸.

Two-photon fluorescence is generated by the same excitation beams used to achieve stimulated Raman scattering (Fig. 1a). We use a 700 nm long-pass dichroic (Edmund Optics, 69-903) to direct the epifluorescence signal towards the dual-channel detector. The emission is filtered with a high-optical-density 700-nm short-pass filter (Thorlabs, FESH0700), split with a 50/50 beam splitter (Thorlabs BSW10R), filtered with a 640/75 nm (Edmund Optics, 67-022) and 590/43 nm band-pass filter (Edmund Optics, 67-020), and detected with two high-sensitivity photomultiplier tube (PMT) detectors (Hamamatsu, H10723-20), respectively. The two emission bands were chosen to match the 640 nm emission peak of PpIX and to be distinct but spectrally close to detect autofluorescence from species such as lipofuscin, NADH and elastin (Fig. 1c).

We detected the output from the PMT detector with two low-frequency analogue-to-digital (ADC) detectors and display the 640 nm signal from PpIX and autofluorescent specimens in red, and

the 590 nm signal from primarily autofluorescent specimens in green (Fig. 1c). As a result, autofluorescence appears in hues of yellow and green depending on the specific emission ratio, while signal in the red channel is primarily driven by the presence of PpIX. We display both the multiwavelength fluorescence and SRH images, and display images from the same optical section side-by-side. The images are linked to enable zoom/pan functionality, allowing for a quick correlation of the images during surgery (Fig. 1b and Supplementary Videos 1–5).

Experimentally, we determined that the PpIX fluorescence was maximal when both the 790 nm and 1,030 nm beams were present in the sample. However, this condition also creates coherent anti-Stokes Raman scattering (CARS) at 641 nm, which coincidentally falls into the 640 nm emission band and overwhelms the weaker PpIX signal. For this reason, we detuned the time delay between the 790 nm and 1,030 nm beams, such that CARS is no longer generated, but TPEF from 790 nm and 1,030 nm is generated independently and measured with the 640 nm detector. We therefore modified the excitation sequence, in which we first image the sample with SRS at 2,845 cm^{-1} , then with SRS at 2,930 cm^{-1} and finally with TPEF, essentially scanning the same image strip three times. The order of this sequence is reversed during consecutive strips to minimize laser tuning and optimize imaging speed (that is, the TPEF is detected first for every other strip). Striping is not visible in the stitched images, indicating that photobleaching does not present a major issue in this acquisition scheme.

Performance of paired SRH/TPEF microscope in standards and tissue

We validated the multimodal imaging system by measuring the fluorescence intensity of serial dilutions of soluble PpIX at known concentrations with a scattering medium that mimics brain tissue³¹ (Fig. 1d) and without a scattering medium (Supplementary Fig. 1) and found that 0.5 $\mu\text{g PpIX ml}^{-1}$ was the threshold for detection (Fig. 1d and Supplementary Fig. 1). As expected, fluorescence intensity increased with increasing PpIX concentration between 0.5 and 221.7 $\mu\text{g ml}^{-1}$ in a scattering medium (Fig. 1d), a range that mirrors the concentration of PpIX clinically encountered in tumour-infiltrated tissue from patients with glioma receiving 5-ALA³².

We then evaluated the ability of the SRH/TPEF microscope to visualize PpIX in brain tumour specimens from patients treated with 5-ALA before resection or biopsy of suspected high-grade glioma. We noted that the SRH/TPEF microscope produced SRH images acquired at the 2,845 cm^{-1} and 2,930 cm^{-1} Raman shifts of comparable character to previous SRH microscopes without the TPEF module, and that the TPEF images could be acquired in corresponding fields of view (Fig. 2). Based on morphologic evaluation, it was possible to visualize the same tissue architecture and cytology in the SRH and TPEF images.

Clinical detection of PpIX in brain tumour tissue typically occurs via microscopes that excite PpIX at ~ 405 nm and detect emission at 600–710 nm via a single-photon excitation fluorescence (SPEF). To ensure the comparable image generation between the conventional SPEF microscopes commonly employed in the operating room and the laboratory and the TPEF-based system we engineered, we used both techniques to image comparable optical sections from the same specimens (Fig. 2j, and Supplementary Figs. 2 and 3) and verified that the pattern of PpIX tissue distribution was comparable between SPEF and TPEF across a series of 30 specimens from 20 patients. We also measured the emission from 569 to 667 nm with 405 nm excitation of sectioned tumour specimens with SPEF and observed a spectral signature consistent with PpIX fluorescence with peak emission at 630 nm (Supplementary Fig. 2). We also performed a photobleaching experiment with SPEF confocal microscopy to confirm that the areas of signal intensity and patterns attributed to PpIX fluorescence decayed with exposure to 405 nm excitation, while the areas with high signal intensity and patterns attributed to autofluorescence do not (Supplementary Figs. 4 and 5).

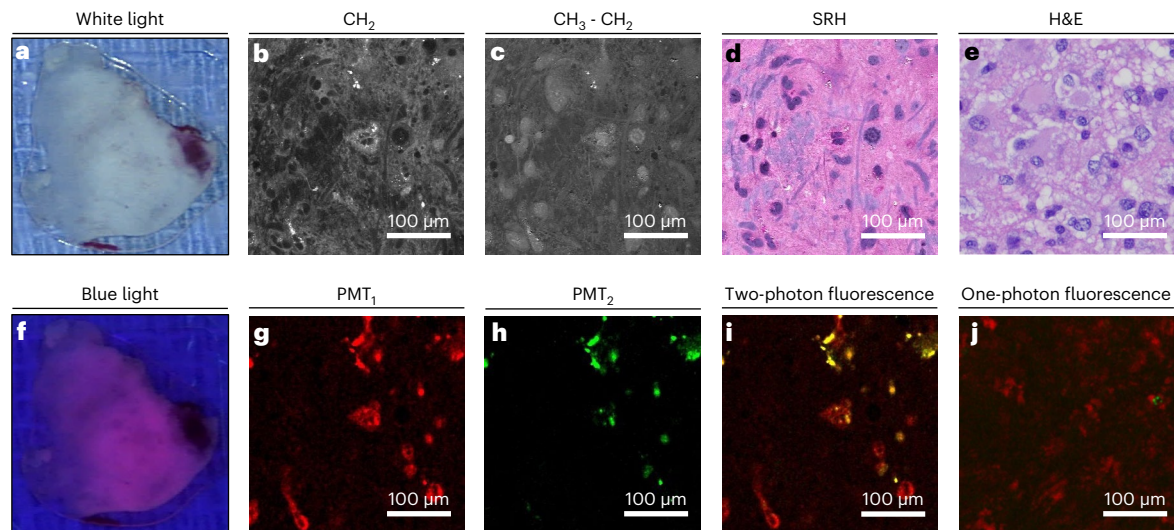


Fig. 2 | Paired SRH/TPEF imaging. **a**, The engineered microscope enables imaging of fresh human brain tumour specimens. **b–e**, For each field of view (100 µm scale), a 2,845 cm^{-1} stimulated Raman scattering image (revealing the distribution of CH_2 bonds) (**b**) and a 2,930 cm^{-1} stimulated Raman scattering image (revealing the distribution of CH_3 bonds) (**c**) are used to generate a stimulated Raman histologic image (**d**) that reveals architecture comparable to conventional H&E staining (**e**). **f–i**, To image the 5-ALA-induced fluorescence

in the same specimen that is visible with a Leica OH5 operating microscope (**f**), 640 nm fluorescence (**g**) and 590 nm fluorescence (**h**) images are assigned to the red and green channels, respectively, to create a multichannel image that highlights the distribution of PpIX and autofluorophores (**i**, **j**). The two-photon excitation fluorescence image (**i**) demonstrates a distribution of PpIX similar to that of a single-photon excitation image (**j**) collected in the same specimen (patient 43).

Measuring the correlation of tissue cellularity and fluorescence

Both neoplastic and non-neoplastic cells contain endogenous fluorophores³³. To ensure that the observed fluorescence in PMT_1 was specific to 5-ALA administration, we imaged tissue from 5 patients with high-grade glioma who had not received 5-ALA before resection. Importantly, in these cases, all fluorescing structures exhibited signal in both channels (rather than solely in PMT_1 , as would be expected for PpIX) suggesting that the fluorescence was due to intrinsic autofluorescent species (Supplementary Fig. 6).

Having validated the performance of the SRH/TPEF imaging system in PpIX solutions and a small number of human control specimens, we sought to systematically evaluate PpIX distribution in a cohort of patients with high-grade glioma treated with 5-ALA ($n = 115$, Supplementary Table 1). The multimodal optical microscope we developed offered a unique opportunity to quantitatively study the relationship between tissue cellularity and fluorescence in high-grade gliomas. To make the best use of the complete microscopic imaging dataset we collected, we utilized QuPath's validated cell-detection module³⁴ to count all cells ($n = 2,504,733$ cells, Fig. 3a) in all imaged specimens (total area of 3,175.5 mm^2) and developed a method for fluorescence quantification in the imaged specimens (Fig. 3b). To quantify the fluorescence of PpIX, the signal from the PMT_2 channel was regularized and subtracted from the PMT_1 channel.

We noted a wide range of cellularity (average: 744 cells per mm^2 , range: 285–1,506 cells per mm^2) and fluorescence intensity among the specimens identified by operating surgeons as lesional and/or fluorescent during surgery (Supplementary Fig. 7). Using regression analysis of our entire dataset, we also noted that there was a weak negative correlation between fluorescence intensity and cellularity ($R = -0.22$, Fig. 3b,c).

Defining patterns of PpIX accumulation in high-grade glioma tissue

Given the unexpected lack of correlation between cellularity and tissue fluorescence, we sought to better understand the distribution of PpIX in high-grade glioma tissue by characterizing the patterns of PpIX accumulation. PpIX appeared to accumulate in distinct patterns

in both extracellular and intracellular spaces. Accumulation occurred to a variable degree both within individual specimens (Supplementary Fig. 8) and among patients (Fig. 4 and Supplementary Fig. 7). To objectively classify the diverse array of patterns of PpIX accumulation, we employed semi-supervised imaging clustering by combining representative and end-to-end learning techniques to identify distinct patterns and quantify their prevalence among patients (Fig. 4a). The semi-supervised clustering revealed a stable separation of five PpIX patterns (Fig. 4b). Generally, there were three patterns of extracellular PpIX accumulation: (1) primarily autofluorescence, (2) diffuse dim PpIX fluorescence or (3) diffuse bright PpIX fluorescence (Fig. 4b,c). Intracellular concentration of PpIX occurred in two patterns, including: (1) fibre-like accumulation (2,577/1,080,412 or 0.2% of fields of views, Supplementary Fig. 9) and (2) cellular accumulation (187,477/1,080,412 or 17.4% fields of view, Supplementary Figs. 10 and 11) (Fig. 4b,c). PpIX pattern prediction heat maps demonstrate the interpretability of our classification and the heterogeneity within a tumour specimen (Fig. 4d). A linear regression was fit to model fluorescence intensity in each patch as a function of the probabilities of the patch belonging to autofluorescence, diffuse dim, diffuse bright, cellular and fibre-like patterns, which explained 74.5% of the variance in fluorescence intensity. There was a significant association between the patterns and fluorescence, with the diffuse bright and fibre-like pattern being positively correlated with fluorescence intensity and the autofluorescence, diffuse dim and cellular patterns being negatively correlated with fluorescence intensity (Supplementary Table 2). To better understand the variability in observed fluorescence, we examined a number of clinical variables with potential influence on the degree of observed fluorescence in study patients: the interval between 5-ALA dosing and specimen imaging (Extended Data Fig. 1), proportion of enhancing tumour, pattern of enhancement and Ki-67 index³⁵. Using a linear fixed effects model, none of these variables were found to correlate with the measured fluorescence intensity of PpIX (Supplementary Table 3).

Identifying the cells concentrating PpIX in human brain tumours

Abundant evidence demonstrates intracellular accumulation of PpIX within glioma cell lines after treatment with 5-ALA in culture^{18–21}.

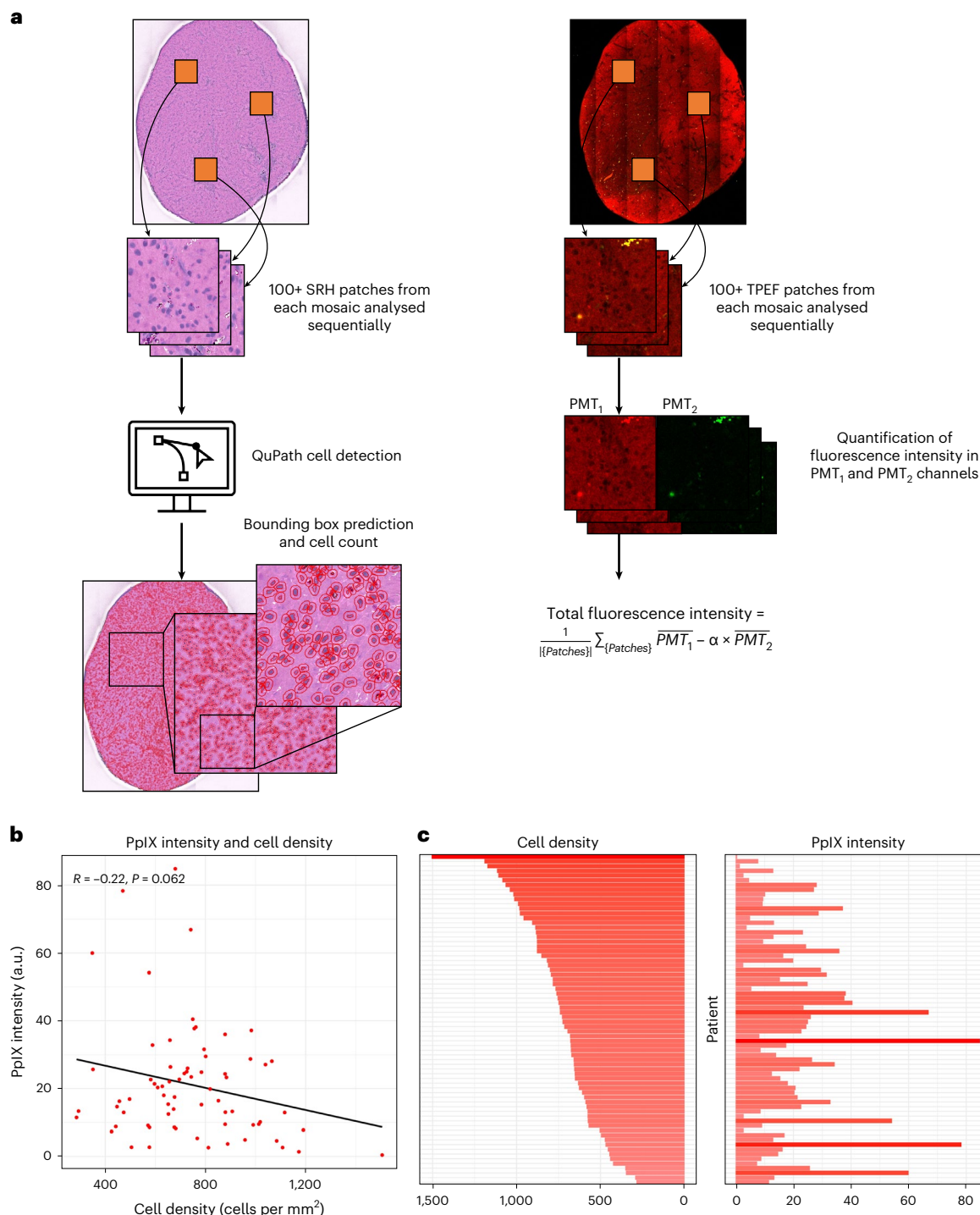


Fig. 3 | Relationship between cellularity and PpIX intensity (a.u.) in human gliomas. a, The QuPath cell-detection module was employed to count each cell in each SRH mosaic and fluorescence was quantified in the PMT₁ and PMT₂ channels to estimate the fluorescence signal attributable to PpIX (for example, patient 9).

b, A linear regression analysis of measured cell density vs PpIX intensity (a.u.) reveals weak correlation. **c,** An alternative visualization of the relationship of cell density to PpIX intensity (a.u.), with individual cases organized by decreasing cellularity to reveal the weak correlation between the variables.

Notably, a definitive correlative study revealing PpIX within glioma cells in human tissues has not been reported. Intriguingly, an approach for PpIX visualization relying on light-sheet microscopy revealed accumulation of PpIX in a small minority of cells, many of which were in the perivascular space³⁶. The SRH/TPEF microscope we developed is particularly well suited for localization of PpIX in brain tumour tissue because it enables comparison of histomorphologic and fluorescent images of the same specimen in the same physical location with sub-micron resolution (Supplementary Videos 1–5).

Although rare in our dataset, we noted that 130,044/2,504,733 cells accumulated PpIX in the cytoplasm and that they generally exhibited morphology more consistent with myeloid cells (such as microglia and macrophages) than with tumour cells, including reniform-shaped nuclei, a granular cytoplasmic appearance and variable cellular shape (including both spherical and elongated forms) (Supplementary Fig. 10). There was a high degree of variability in the abundance of cells with high intracellular PpIX fluorescence intensity among and within patients. However, cells with high intracellular PpIX fluorescence

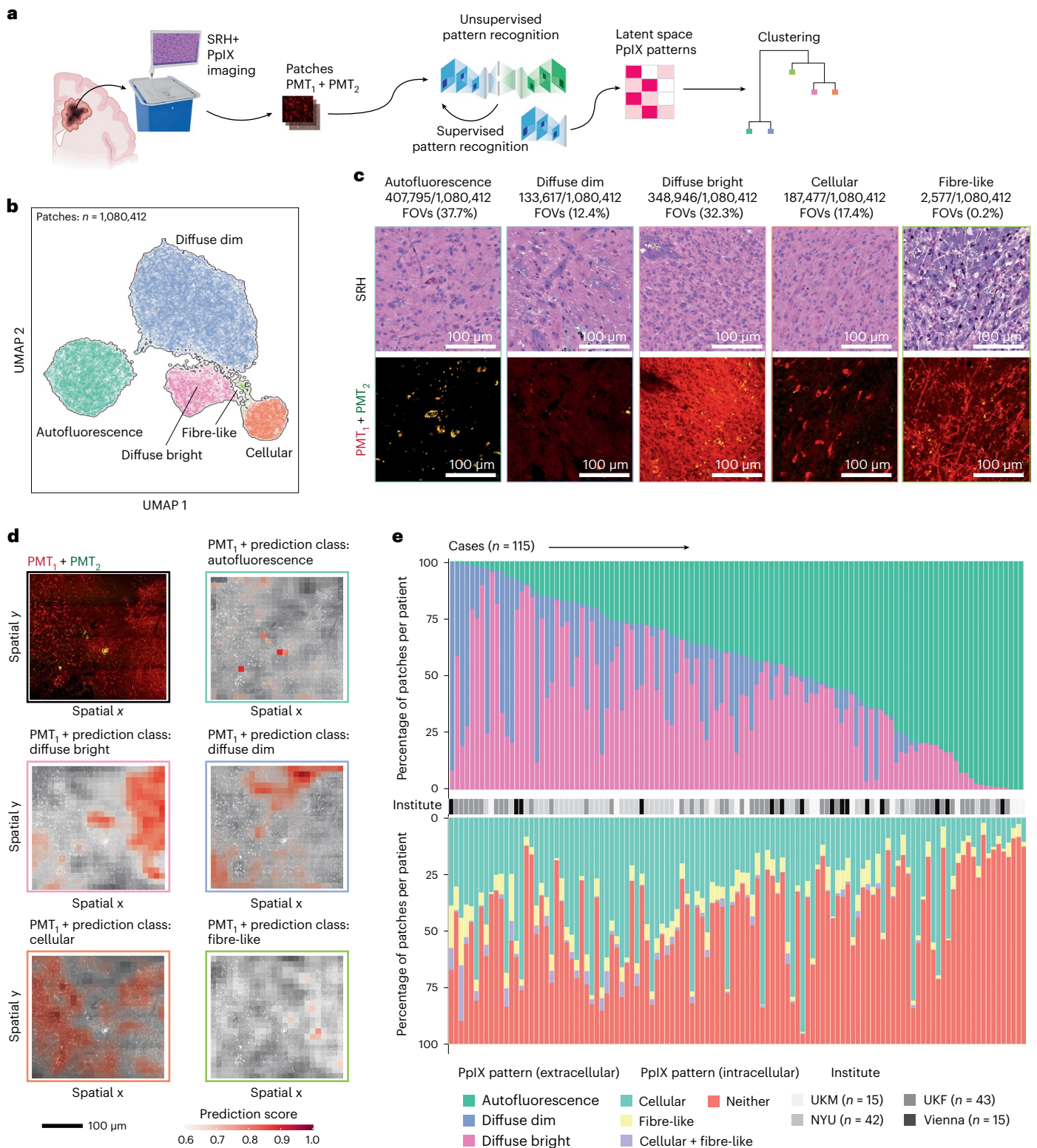


Fig. 4 | Semi-supervised analysis of PpIX patterns in human gliomas. **a**, Tissue specimens from patients undergoing biopsy or resection for high-grade glioma were imaged using the SRH/TPEF microscope. Patches of the TPEF images were generated and used to train a convolutional neural network (CNN) encoder using semi-supervised learning for TPEF image feature embedding. The dimensionality of the latent space of the TPEF image embeddings was reduced using UMAP and the TPEF image embeddings were clustered using *K*-nearest neighbours (created with BioRender.com). **b**, Dimensional reduction of CNN-based deep-learning latent space via UMAP, highlighting the various PpIX patterns. Each point on the UMAP corresponds to a patch, with colours denoting distinct patterns. **c**, Exemplary images showcasing each identified PpIX pattern. The upper row

presents SRH images, while the lower row displays PMT_1 (red) and PMT_2 (green) channels. **d**, A sample image featuring PMT_1 (red) and PMT_2 (green) channels (upper left), with corresponding pattern prediction heat maps (gradient: white, low score; red, high score). The heat maps are superimposed on a greyscale image of the PMT_1 channel is displayed, framed by the colour indicative of the corresponding pattern. **e**, Stacked bar plots depicting pattern distribution among patients. Colours represent different patterns. The upper bar plot exhibits the percentage distribution of autofluorescence, diffuse dim and diffuse bright patterns. Conversely, the lower bar plot shows the percentage of cellular, fibre-like or mixed cellular and fibre-like patterns. The middle row denotes the neurosurgical centres where the imaging was performed.

intensity were observed either along blood vessels (Supplementary Fig. 11) or infiltrating among tumour cells in 110/115 patients in a pattern consistent with the known distribution of myeloid cells within high-grade gliomas³⁷.

Cytologic and histoarchitectural features led us to suspect that cells concentrating PpIX intracellularly were myeloid cells, a subset of tumour cells or pericytes. We therefore employed immunostaining for markers of M2-polarized macrophages (CD163+), astro-glial derived cells such as reactive astrocytes and tumour cells (GFAP+), and pericytes (SMA+) in 5 cases (Extended Data Fig. 2)³⁸. In these cases, we noted that the abundance and morphology of cells with intracellular PpIX accumulation mirrored that of CD163+ cells in the imaged specimens. We then evaluated the abundance of CD163 in the 45 study patients in which imaged tissue was available for CD163+ immunohistochemistry by comparing the degree of CD163 positivity to the quantity of cells concentrating PpIX within their cytoplasm. The abundance of cells concentrating PpIX within their cytoplasm was closely associated with quantified CD163 positivity (Extended Data Fig. 2). The difference in the number of cells concentrating PpIX in the cytoplasm was greatest between tissues with the greatest CD163 positivity and those with the least CD163 positivity ($P = 0.002$) but remained significant even when tissues with moderate CD163 positivity were compared to those with the least CD163 positivity ($P = 0.02$; Extended Data Fig. 2).

5-ALA-induced fluorescence in non-glial brain tumours has been previously reported^{39–43}. Consequently, we hypothesized that PpIX might accumulate within CD163+ cells in non-glial tumours. In addition, there have been sporadic reports suggesting CD163 expression by glioma cells⁴⁴. We examined tissue from three patients in whom 5-ALA was administered given a suspicion for high-grade glioma but were ultimately diagnosed with diffuse large B-cell primary central nervous system lymphoma. As observed in the glioma patients in the study, in tissue from central nervous system lymphoma biopsies, there was abundant intracellular accumulation of PpIX in cells that mirrored the population of CD163+ macrophages, rather than in the neoplastic B lymphocytes, both in quantity and morphology (Extended Data Fig. 3).

Resolving the molecular characteristics of PpIX fluorescence patterns in accumulating cells

We hypothesized that the diverse PpIX patterns are connected to the spatial cellular and transcriptional heterogeneity in glioblastoma^{45,46}. To explore the underlying cellular and transcriptional heterogeneity resulting in diverse PpIX patterns, we designed a multi-omic strategy that synergistically incorporates SRH/TPEF imaging and spatially resolved transcriptomics ($n = 6$). This approach facilitates congruent PpIX imaging and transcriptomics, thereby providing a robust method for investigating the related biological functions. Specifically, tissue specimens were imaged using the SRH/TPEF microscope and subsequently embedded in optimal cutting temperature (OCT) compound and processed for array-based spatial transcriptomics at a depth analogous to the SRH/TPEF microscope imaging acquisition, and both H&E and PpIX images were co-registered using affine transformation (Fig. 5a).

The PpIX fluorescence patterns within tissue imaged via TPEF were ascertained through a pretrained residual neural network (Fig. 4a). These fluorescence patterns were compared to the distribution of various cell types unveiled through the single-cell deconvolution of spatial transcriptomic data (Fig. 5b). The cellular PpIX fluorescence pattern aligned well with that of myeloid cells, while there was poor overlap with the distribution of malignant cells (Fig. 5b). Gene ontology analysis of differentially expressed genes in disparate regions indicated that the cellular PpIX fluorescence pattern robustly correlates with antigen presentation and processing, indicating immunologically enriched niches. (Fig. 5c). Moreover, the fibre-like pattern was correlated with the abundance of astrocyte-like tumour cells, which are implicated in the formation of tumour networks. Functional enrichment analysis substantiated the association between fibre-like patterns, hypoxia

response and metabolic stress signatures (Fig. 5c). Quantification of the average percentage of each cell type for each spatial transcriptomic spot revealed that myeloid cells were the predominant cell type in the cellular and mixed cellular/fibre-like PpIX fluorescence patterns. In contrast, astrocyte-like tumour cells were the predominant cell type in the fibre-like and diffuse bright PpIX fluorescence patterns (Fig. 5d).

Protoporphyrin IX is enriched in the myeloid cell population

To confirm the observation of elevated PpIX fluorescence intensity in macrophages, we expanded our analysis of integrative spatially resolved multi-omics data, leveraging an external dataset of integrated spatially resolved metabolomics (matrix-assisted laser desorption/ionization Fourier transform ion cyclotron resonance mass spectrometry (MALDI-FTICR-MSI)) and transcriptomics (Visium 10X) that was acquired from six patients with GBM who were treated with 5-ALA⁴⁵ (Fig. 6a,b). PpIX is metabolized from 5-ALA via an intermediate compound, coproporphyrinogen III (CpPIII). We hypothesized that active PpIX metabolism is marked by the simultaneous expression of the haem biosynthesis enzymes and the accumulation of intermediate metabolites. Spatial correlation of the recently described regional transcriptional expression patterns (reactive immune, reactive hypoxia, spatial opc, radial glia and neuronal development⁴⁵) with both 5-ALA intermediate metabolites and gene expression of haem biosynthesis enzymes revealed high co-localization of 5-ALA metabolism with immune active regions (reactive immune) (Fig. 6c). The ‘reactive immune’ regions are marked by a high content of mesenchymal-like malignant cells with CD163/Haem oxygenase 1 (HMOX1) immunosuppressive macrophages^{47–49}. HMOX1 has been shown to be an important marker of increased haem metabolism⁵⁰, which also suggests a key role of this subpopulation of macrophages in PpIX metabolism. We noted that this observation was also consistent with the finding that myeloid cells, unlike CD45 negative cells, have a substantially enhanced PpIX fluorescence signal⁵¹.

Since Visium technology lacks single-cell resolution (55 μm spot size), we performed single-cell deconvolution using the state-of-the-art robust cell-type deconvolution (RCTD)⁵² and the GBMap reference dataset containing ~1 million cells⁵³ to verify the accumulation of PpIX in macrophages on a cellular level. The inherent heterogeneity of PpIX accumulation in the external dataset specimens enabled us to compare cellular composition across areas of low and high PpIX accumulation (Fig. 6d)⁴⁵. RCTD provided cell-type likelihood scores for each spot, which were spatially correlated with the expression of enzymes (in red) and metabolite intensities (in blue) (Fig. 6c and Extended Data Fig. 4a). Myeloid cells, particularly immunosuppressive tumour-associated macrophages and inflammatory microglia, demonstrated a significant correlation with PpIX intensities and haem biosynthesis enzyme expression (Fig. 6d). Astrocyte-like malignant cells also exhibited enhanced PpIX intensities and haem biosynthesis enzyme expression. These two findings suggest that macrophages are not the only cells metabolizing 5-ALA in glioblastomas, but that macrophages metabolize 5-ALA to a greater extent relative to other cell types. To verify that regions with high myeloid content exhibited higher PpIX, we extracted mass spectra regions of interest from both high CD163 expression and non-expressing control regions, confirming that higher PpIX intensity was present in macrophage-enriched regions ($P_{\text{adj}} = 0.0032$) (Extended Data Fig. 4c,d).

To further validate our findings on an external, publicly available dataset, we utilized bulk RNA-seq data obtained from PpIX-positive cells separated with fluorescence-activated cell sorting (FACS) (Fig. 6e)⁵⁴. Cell-type deconvolution from bulk data by multisubject single-cell deconvolution (MuSiC)⁵⁵ and the GBMap dataset demonstrated enrichment of myeloid and oligodendroglial lineages among PpIX-positive cells. We focused RNA-seq data analysis on the tumour infiltration zone (Fig. 6f and Extended Data Fig. 4d,e) because it contains both malignant and non-malignant cells (Fig. 6f and Extended Data Fig. 4d,e). Notably, malignant cells represented only 5% of the PpIX-positive cells isolated

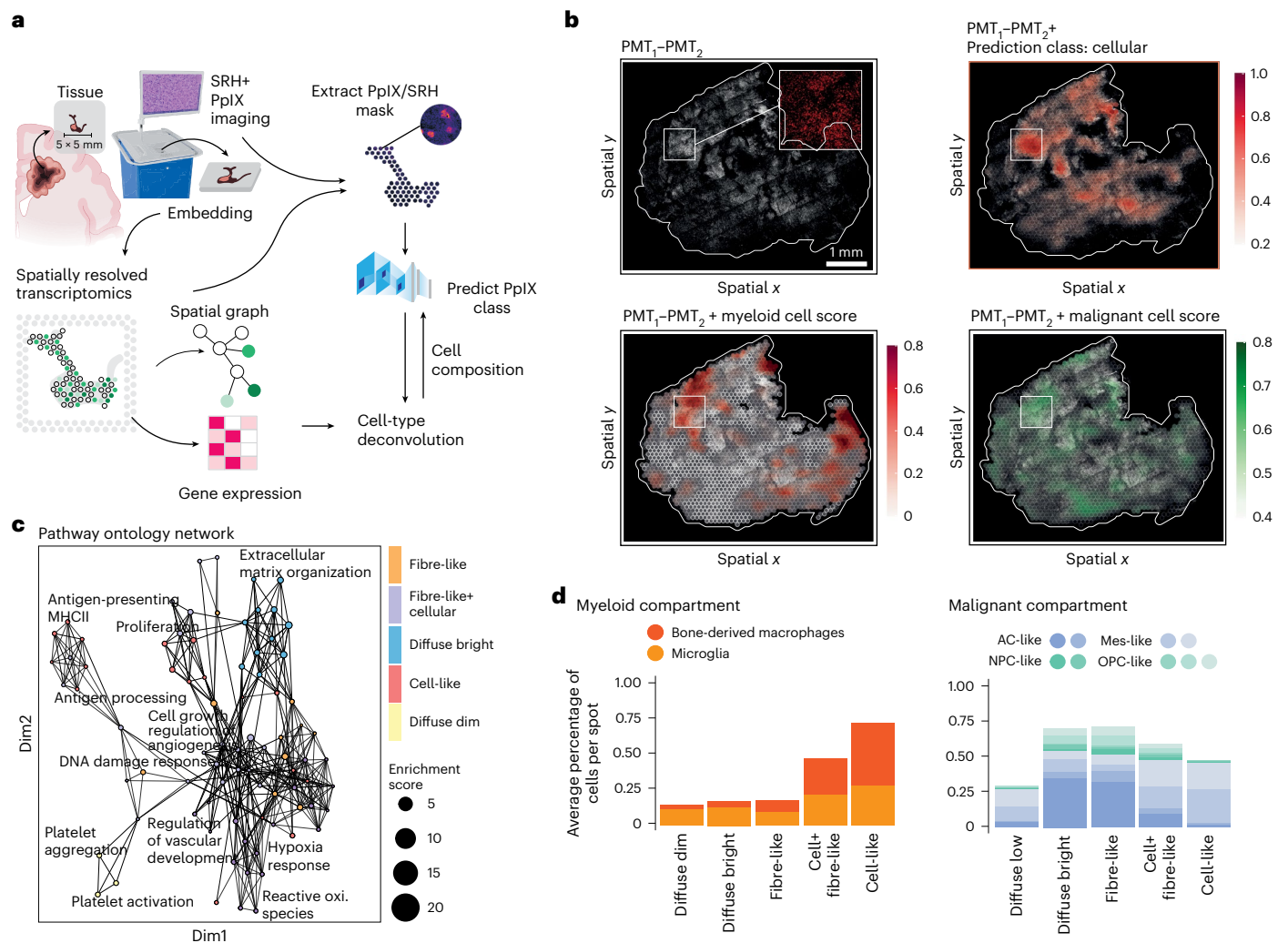


Fig. 5 | Molecular exploration of PpIX patterns in PpIX-accumulating cells.

a, Schematic of the PpIX pattern molecular exploration workflow. Post imaging, tissue specimens are embedded, sliced and subjected to spatially resolved transcriptomics. The resultant spatial transcriptomics images are aligned to the TPEF (PMT₁ + PMT₂ channels) images using affine transformation. Predicted PpIX patterns, informed by a trained ResNet, are then compared with molecular downstream analyses, which include differential gene expression, spatial clustering and single-cell deconvolution (created with BioRender.com).

b, Representative examples featuring the PMT₁-PMT₂ channel in greyscale (upper left), with white lines demarcating tissue borders. The upper right exhibits a heat map of a cellular pattern (gradient: white, low score; red, high score). Each heat map is superimposed on a greyscale image of the PMT₁-PMT₂

channel is presented. The outlined box depicts a region of interest with a view of the coloured TPEF image. **c**, Differential gene expression between PpIX fluorescence patterns was conducted. The uniquely and significantly expressed genes for each PpIX fluorescence pattern were utilized in subsequent GSEA to annotate biological functions. The GSEA is depicted as a graph where nodes are coloured according to the corresponding PpIX fluorescence pattern. Edges denote pathway similarity and node size is proportional to the enrichment score of each pathway. **d**, Spatial transcriptomic data were deconvoluted to infer the single-cell composition of each spot. Stacked bar plots display the cell-type composition of various PpIX fluorescence patterns, with myeloid cells shown on the left and malignant cell subpopulations shown on the right.

from infiltration zone tissue, which was predominantly composed of tumour-associated macrophages and oligodendroglial cells (Fig. 6f). The cellular composition of the PpIX-positive fraction was further investigated by inferred copy number alterations demonstrating the lack of the characteristic gain of chromosome 7 and loss of chromosome 10 in PpIX-positive cells (Extended Data Fig. 4f,g and Supplementary Fig. 12). In conclusion, our data suggest that 5-ALA is metabolized at a high rate by myeloid cells and accumulates in myeloid cells, a finding that is reproducible across spatial transcriptomic, metabolomic and RNA-seq datasets (Supplementary Fig. 13).

Discussion

Improving the safety and accuracy of tumour resection is a long-standing focus in surgical oncology. Given the challenge of delineating tumour from adjacent brain, intense effort has been dedicated

towards developing technologies such as 5-ALA fluorescence guidance (both with operating microscopes and handheld devices) to enable better visualization of tumour margins in glioma surgery^{23,56,57}. Based on definitive improvements in completeness of resection in high-grade glioma surgery shown in ref. 3 and the concept of metabolic targeting of abnormalities in the haem biosynthesis pathway specific to glioma cells⁵⁸, 5-ALA has become a widely used adjunct in the field of neurosurgical oncology.

Regardless of the precise mechanism of accumulation of PpIX, a fluorescent metabolite of 5-ALA has been previously hypothesized to accumulate specifically in tumour cell cytoplasm, creating visible fluorescence. The evidence for glioma cell-specific accumulation is primarily based on in vitro studies and studies in animal models. While there are several studies that correlate observed fluorescence with the density of tumour cell infiltration in glioma specimens¹, there is a

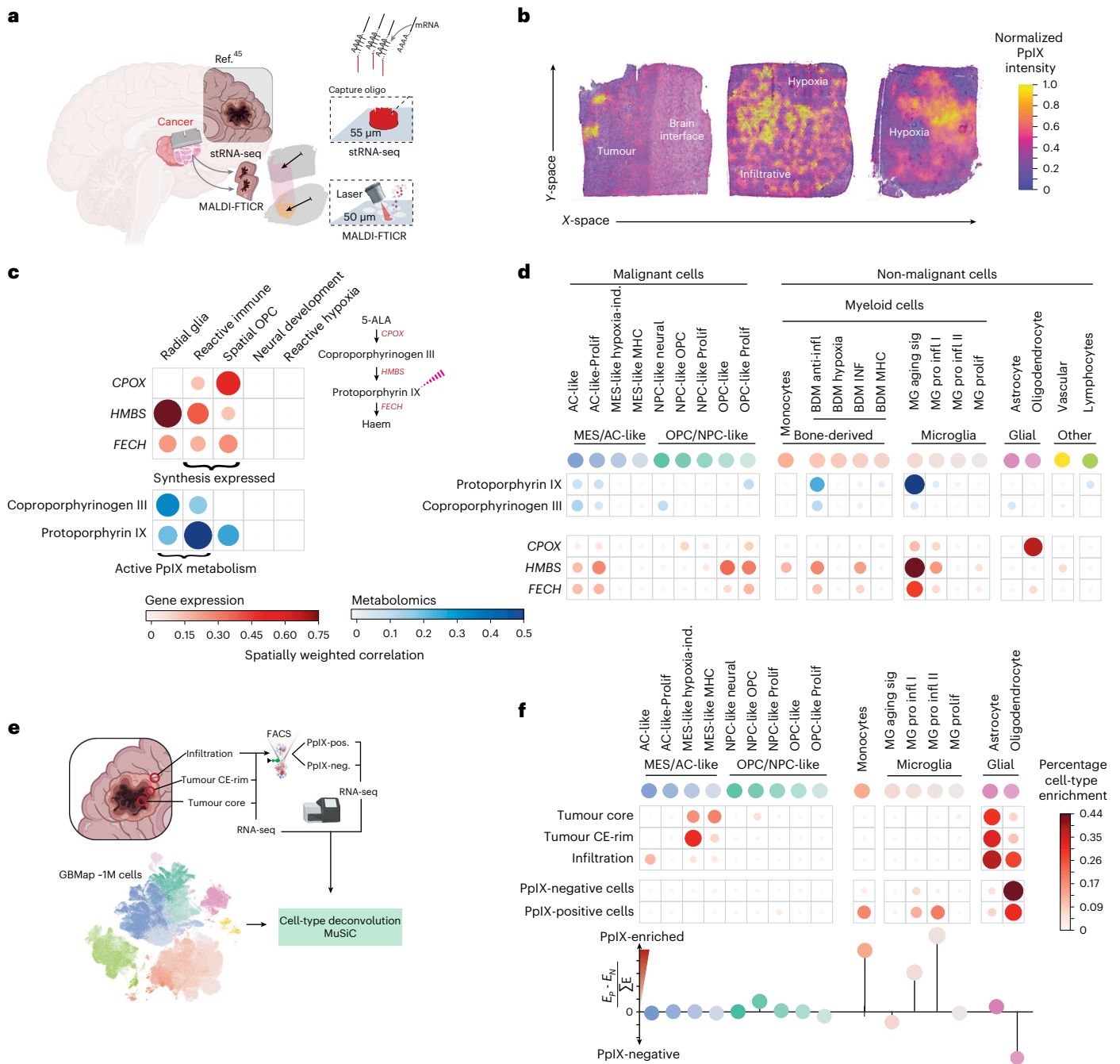


Fig. 6 | Transcriptomic and metabolomic analysis of PpIX-rich cells in external datasets. **a**, Illustration of the integration of the spatial transcriptome RNA sequencing (stRNA-seq) and MALDI-FTICR, utilizing sample-wise comparison (created with BioRender.com). **b**, Examples of PpIX intensity in infiltrative areas and normal brain surface (left), juxtaposed with PpIX intensity in cellular tumour regions (middle) and hypoxia-associated tumour areas (right). **c**, Dot plot depicting the estimated spatial correlation of enzyme expression (red) and metabolites (blue) versus the enrichment of spatial transcriptional

programmes in six patients. **d**, Dot plot showcasing the spatially weighted correlation analysis of enzymes (red) and metabolites (blue) with cell-type likelihood scores across six patients. **e**, Illustration of ref. 54 dataset integration with the GBMap single-cell dataset. **f**, Top: percentage representation of selected cell-type enrichments. Bottom: the differences in cell-type enrichments between PpIX-positive and negative samples. E denotes the cell-type enrichment score and the y axis displays the score difference $E(\text{PpIX}+) - E(\text{PpIX}-)$ divided by the sum of cell-type enrichment scores.

paucity of published evidence of 5-ALA-induced tumour fluorescence in human brain tumour specimens²⁴. In addition, fluorescence has been reported in non-infiltrated tissue in patients with glioma¹⁰, perilesional tissue in patients with metastatic tumour, inflammatory and dysplastic brain lesions^{59,60}. Moreover, the accumulation of fluorescent protoporphyrins after 5-ALA administration is well documented in non-glioma tumours, both inside⁶¹ and outside of the brain^{62,63}. Importantly, there is a growing body of work demonstrating that myeloid cells are labelled

with PpIX and correlate with PpIX signal intensity^{51,64}, which we have confirmed in this study using multiple modalities and internal and external datasets. Bone marrow-derived macrophages increased in concentration in 30 tissue samples with intense PpIX-induced fluorescence⁵¹. Also, many cell types exhibit PpIX-induced fluorescence in glioma, and glioma cells are not necessarily the predominantly labelled cell type in some tumours, with myeloid cells possibly being substantially brighter⁶⁴.

To better understand the distribution of PpIX in brain tumours at the cellular level, we modified a bedside histologic imaging system that we previously developed for intraoperative use. This system enabled us to match virtual H&E and two-photon fluorescence images at the same location in the exact same optical tissue section, with submicron resolution in fresh unprocessed human brain tumour specimens. The impact of this unique optical system was unexpected as it demonstrated that PpIX accumulates both in the intracellular and extracellular spaces, and that intracellular accumulation was most avid in tumour-associated macrophages rather than tumour cells—findings that were validated on an internal dataset of spatial transcriptomics and three external datasets (that is, spatial transcriptomics, metabolomics and RNA-seq). These results are not consistent with the dogma that visible fluorescence in gliomas is driven by intracellular tumour cell accumulation of PpIX and should encourage a reconsideration of existing hypotheses on the mechanistic basis of observed PpIX accumulation within brain tumours.

5-ALA is reported to selectively accumulate within glioma cells due to their downregulation of ferrochelatase, but may also be impacted by dysregulation of ALA dehydratase, porphobilinogen deaminase, coproporphyrinogen oxidase, haem oxygenase, nitric oxide synthase as well as factors such as cell density and hypoxia⁵⁷. While future work will be required to generate new theories of how PpIX accumulation occurs in brain tumours, existing evidence suggests that accumulation of PpIX is most strongly influenced by the permeability of the blood–brain barrier²³.

An important limitation of this study is that we focused on brightly fluorescing and/or lesional-appearing specimens taken predominantly within areas of pathologic, tumour-induced blood–brain barrier breakdown. It is likely that additional insight into the tissue distribution of PpIX in and around brain tumours will result from a systematic comparison of tissue sampled from uninvolved/minimally involved brain tissue (presumably with intact blood–brain barrier), the tumour periphery and viable core (where the blood–brain barrier is dysfunctional). Another important limitation of this study is that the estimation of PpIX intensity in our specimens correlates with that seen in SPEF methods but may be impacted by the spectral properties of the TPEF microscope we engineered. Specifically, the microscope we developed is primarily designed to detect the physicochemical state of PpIX that emits at 634 nm, rather than the state that emits at 620 nm. However, the 620 nm signal would show up in both PMTs. Notably, there was no appreciable 620 nm signal within tumour cells to suggest PpIX accumulation in a pattern distinct from that observed with measured signal in PMT₁.

In addition to tumour cells, PpIX appears to accumulate in a large subpopulation of tumour-associated macrophages, sometimes to an even greater extent than within tumour cells depending on the tumour specimen. The varied source and extent of visible fluorescence underscores the challenge of interpreting fluorescence during surgery and the importance of integrating anatomic, functional, imaging and gross visual cues when deciding to resect or preserve tissue encountered during surgery.

The discrepancy between the expected and observed location of PpIX on a cellular level speaks to the importance of assessing the expanding library of clinical fluorophores designed for use in fluorescence-guided surgery with optical systems that enable precise biodistribution studies. Through the use of an imaging system where tissues and individual cells can be microscopically assessed via both structural and fluorescence-based imaging modalities, it will be possible to verify fluorophore targeting rather than inferring it from low-resolution imaging methods or correlations between measured fluorescence and tissue cellularity.

The unexpected ability of the SRH/TPEF microscope to reveal intracellular PpIX accumulation within tumour-associated macrophages is notable given the central role of the immune system in

tumourigenesis⁶⁵, a current focus in the field of neuro-oncology on the development of antitumour immunomodulatory approaches^{66,67} and the documented prognostic value of myeloid cells in patients with GBM⁶⁸. Histiocytes encompass an array of myeloid immune cells, including monocyte-derived macrophages and microglia, and have the capacity to promote and interfere with glioma growth⁶⁹. Recent evidence suggests a critical role for myeloid cells in patients with GBM who respond to anti-PD-1 immune checkpoint inhibitors⁷⁰. Additional investigation is underway in our laboratory to better characterize the subset of immune cells that concentrate PpIX in high-grade glioma. Ultimately, PpIX may become a valuable microscopic imaging agent for assessing macrophage physiology in brain tumours at the time of diagnosis and, possibly, in the setting of immunotherapy.

Outlook

Combining stimulated Raman histology and two-photon fluorescence microscopy on a single optical system offers a unique means of simultaneously visualizing tissue architecture and fluorophore distribution. By using this system, we noted that PpIX accumulates in tissue specimens from patients with 5-ALA-treated GBM, with variable distribution across the intracellular and extracellular tissue compartments. The finding that intracellular PpIX accumulation may occur within tumour-associated macrophages creates a new avenue for visualizing this critically important component of the tumour–immune microenvironment.

Methods

Study design

The inclusion criteria for this study were as follows: (1) adult males and females; (2) patients undergoing brain-tumour resection at the NYU Langone Medical Center, the Medical University of Vienna, the Münster University Hospital, or the Medical Center - University of Freiburg (3) patients (or designee) who provided informed consent or where a waiver of consent applied; (3) patients who received 5-aminolevulinic acid 2–12 h before tumour resection; (4) patients with excess tumour tissue resected beyond that needed for diagnosis; and (5) patients with a final diagnosis of a high-grade glioma.

The sample size was estimated at 115 patients to ensure adequate representation of all major tumour types for analysis and on the basis of the design of previous studies comparing SRS and H&E. The central goals of this study were: (1) to build and verify a clinical microscope capable of performing both stimulated Raman spectroscopy and two-photon excited fluorescence microscopy; (2) to judge whether 5-aminolevulinic acid accumulated in tumour cells, on the basis of diagnostic histopathologic (SRH) images and TPEF images; and (3) to determine in which cells 5-aminolevulinic acid accumulated. We began by collecting up to four biopsies from neurosurgical patients undergoing tumour resection. Each specimen was imaged with the SRS and TPEF microscope immediately after removal.

Tissue collection and imaging

Tissue was collected at NYU Langone Medical Center according to the NYU Langone Institutional Review Board (IRB)-approved protocol (IRB S19-01931), at the Medical University of Vienna according to the Medical University of Vienna-approved IRB protocol (419/2008 - Ethics Commission Medical University Vienna), at the Münster University Hospital according to the Münster University-IRB protocol (2007-420-f-S and 2017-707-f-S), and at the Medical Center - University of Freiburg according to the University of Freiburg IRB protocol (23-1175-S1). Tissue was imaged using the NIO Imaging System (Invenio Imaging) at a standard depth of 10 μm from the surface of the compressed tissue specimen and, after imaging, sent to the clinical pathology laboratory for downstream analysis. In a subset of cases with sufficient tissue beyond that needed for clinical diagnosis, tissue was immersed in saline or fixed in formalin for CD163 staining and/or single-photon

microscopy. Single-photon fluorescence images of specimens utilizing a standard confocal fluorescence microscope (Zeiss LSM880) and SRH/TPEF images were obtained on tissues imaged with the NIO Laser Imaging system (Invenio Imaging).

Imaging specimens with TPEF and SPEF

Tumour specimens to be imaged with the NIO Laser Imaging system were first split in half via surgical blade and divided into two portions: one portion to be imaged with paired SRH and TPEF microscopy, and the other portion to be imaged with confocal SPEF microscopy. The confocal-imaged portions were sealed without fixation on a standard glass microscope slide under a #1.5-thickness coverslip. All confocal images were collected immediately on an inverted Zeiss LSM880 laser scanning confocal microscope with GaAsP detectors. Scans were performed with either a Plan-Apo $\times 20/0.8$ M27 objective. Fluorescence was excited using a 405 nm laser with a pinhole diameter of 1 Airy Unit and emission was acquired in Lambda scanning mode from 502 to 689 nm with 9 nm width increments. Both single fields and tile scans were collected; tile scans were stitched in Zen Black (Carl Zeiss).

SPEF and TPEF photobleaching of PpIX

SPEF images were collected on a Zeiss LSM 800 laser scanning confocal microscope in Lambda scan mode across 502 to 689 nm with 9 nm wavebands using 405 nm excitation. Wavelengths to plot over time from Lambda mode were selected at 636 nm (red) and 556 nm (green). A total of 153 samples was collected over a period of 375 s. TPEF images were collected on a NIO Laser Imaging system equipped with dual time-delay detuned 720 and 1,020 nm lasers for two-photon excitation. Fluorescence emission was collected with a 640 nm centre wavelength/75 nm bandwidth filter (red) and a 590 nm centre wavelength/43 nm bandwidth filter (green). A total of 16 samples was collected over a period of 375 s. The mean fluorescence over time was plotted in Fiji (2.3.0) with the plot Z-axis profile function. R^2 values were calculated by fitting a logarithmic function in Fiji (2.3.0).

TPEF imaging of PpIX serial dilutions

To provide a reference for fluorescence that was detected on TPEF images, we performed a dilution series of PpIX measured with TPEF. Pure PpIX was dissolved in 5% Tween-20 phosphate buffered saline (PBS) to create serial dilutions ($0-125 \mu\text{g ml}^{-1}$), each with a 50% reduction in the concentration of PpIX. The PpIX serial dilution solutions were imaged under 410 nm excitation and imaged with the SRH/TPEF microscope. This serial dilution procedure was repeated three times and each dilution was measured three times for internal and external reproducibility. The fluorescence intensity was computed for each serial dilution and the average fluorescence intensity with 95% confidence intervals was calculated and plotted.

To provide further reference for fluorescence that was detected on TPEF images in a scattering medium, PpIX (Frontier Scientific) stock was prepared in dimethylsulfoxide (DMSO) (Fisher Bioreagents), milk (Cream-O-Land Dairy, 3.5% milk fat) and India ink (StatLab Medical) solution, and serially diluted to a solution of DMSO, 1.6% milk fat and $0.3 \mu\text{l ml}^{-1}$ India ink as described in ref. 31. Twenty three serial dilutions were prepared, starting at a concentration of $748.2 \mu\text{g ml}^{-1}$ and ending at a concentration of $0.1 \mu\text{g ml}^{-1}$, decreasing each serial dilution's concentration by a factor of 1.5. A control dilution (that is, no PpIX) was prepared with only DMSO, milk and India ink, and another control dilution was prepared with only DMSO. A second series of the same serial dilutions was prepared from the previous PpIX stock to the same liquid optical phantom concentrations with the addition of 0.5% Tween 20 (Sigma-Aldrich). A control dilution (that is, no PpIX) was prepared with only Tween, DMSO, milk and India ink, and another control dilution was prepared with only Tween and DMSO. Optical phantoms and concentrations were selected on the basis of mean brain reduced scattering and absorption coefficients as compared to the reduced

scattering coefficient and absorption coefficient of 3.5% milk and India Ink, respectively, as described in ref. 71. Tween 20 concentration was selected according to the observed influence on emission intensity of PpIX fluorescence described in ref. 31.

Fluorescence quantification and cell counting

Each SRH and TPEF image pair was manually reviewed by D.J., and non-diagnostic regions of each image (for example, blood and necrotic tissue) were removed, as these contain structures appearing like cells that can add noise to automated cell counting in the virtual H&E images and have high autofluorescence that can add noise to the PpIX signal in the TPEF images. A sliding window algorithm was applied to generate 300×300 pixel patches from these cropped virtual H&E and TPEF images.

To measure the fluorescence signal of endogenous fluorophores captured by the PMT_1 and PMT_2 filters, we computed the ratio of fluorescence in the PMT_1 channel and the fluorescence in the PMT_2 channel for each of the negative control cases. The mean PMT_1 to PMT_2 ratio for the negative control cases was used as a regularization term to remove the signal from endogenous fluorophores in the PpIX quantification

$$\alpha = \frac{\sum_{\{\text{negative controls}\}} \frac{\text{PMT}_1}{\text{PMT}_2}}{|\{\text{negative controls}\}|} \quad (1)$$

The PpIX fluorescence was quantified for each TPEF patch by subtracting the averaged and regularized PMT_2 channel from the average of the PMT_1 channel. The case-level fluorescence intensity was calculated as the average fluorescence intensity of all tissue imaged in the case

$$\text{caseFluorescenceIntensity} = \frac{\sum_{\{\text{TPEF patches}\}} (\overline{\text{PMT}_1} - (\alpha \times \overline{\text{PMT}_2}))}{|\{\text{TPEF patches}\}|} \quad (2)$$

Each patch from the virtual H&E and TPEF images was analysed using QuPath's watershed cell detection for Brightfield H&E images, which detected cells with a minimum area of $50 \mu\text{m}^2$ and a maximum area of $400 \mu\text{m}^2$. The density of each patch was calculated as the number of cells in the patch divided by the area of the patch in μm^2 . The case-level cell density was calculated as the total number of cells in the case divided by the total area of tissue imaged in the case

$$\text{caseCellDensity} = \frac{\sum_{\{\text{H\&E patches}\}} |\{\text{cells}\}|}{\sum_{\{\text{H\&E patches}\}} \text{area(patch)}} \quad (3)$$

A linear regression and its correlation coefficient were computed to map patients' average cellular density to their average fluorescence intensity.

CD163 density analysis

A representative section of formalin-fixed paraffin-embedded (FFPE) tissue was subjected to immunohistochemical analysis using a clinically validated monoclonal antibody against CD163 (MRQ-26, Roche Diagnostics) to detect cells of monocyte/macrophage lineage within all cases that underwent SRH/TPEF imaging. The immunohistochemistry was reviewed by a pathologist (M.M.-E.), who is a board-certified anatomical and clinical pathologist, and for semi-quantitative analysis, tumour-associated CD163-positive cells was categorized into three groups: low, medium and high. CD163 expression was quantified as the percentage of positive cells in a section as follows: low, $<10\%$ positive cells; medium, $\geq 10-60\%$ positive cells; high, $>60\%$ positive cells. Furthermore, CD163 immunoreactive cells were evaluated for focal or diffuse infiltration within the tumour tissue.

Semi-supervised pattern analysis

For semi-supervised investigation of PpIX images, hybrid methodology merging end-to-end and reconstructive learning was developed.

A sliding window algorithm was applied to generate 160×160 pixel patches from each TPEF image. An autoencoder model was trained using the 160×160 pixel patches with a ResNet-backed architecture. This model encompassed a latent space dimension comprising 128 latent features. To fine-tune the latent representation of defined patterns, iterative optimization was used to synergize end-to-end learning of latent space clustering (kNN) with a preset k -value of 5 and the pretrained ResNet as the encoder within the autoencoder framework. This step effectively optimized the latent representation, ensuring efficient capture of relevant patterns in the PpIX images. In the subsequent phase, ~100,000 patches (~10% of the total 854,957 patches) were manually segmented according to the following patterns: 'autofluorescence', 'diffuse dim', 'diffuse bright', 'cellular' and 'fibre-like'. The encoder was refined and further trained on the basis of this 10% segmented dataset. Performance was evaluated using a validation dataset composed of ~20% segmented data (225,455 patches). Training was carried out over 500 epochs, with the end-to-end component being performed over 200 epochs.

Pattern analysis and clustering

For further analysis, the latent space of the trained ResNet autoencoder was extracted and clustered by kNN clustering as well as hierarchical clustering (`knn = KNeighborsClassifier().fit(latentspace)`). For visualization and dimensional reduction, we trained a uniform manifold approximation and projection (UMAP)⁷² model using the `umap-learn` package (`embedding = umap.UMAP(n_neighbors=5).fit_transform('latentspace')`).

Modelling fluorescence intensity as a function of fluorescence pattern

A linear regression modelling the fluorescence intensity observed in a patch as a function of the probabilities of the patch belonging to the autofluorescence, diffuse dim, diffuse bright, cellular and fibre-like patterns as determined using the semi-supervised machine learning model. This model was used to assess the association between each fluorescence pattern and fluorescence intensity. All analyses used a significance level of 0.05 and were conducted in R.

Tissue embedding and imaging

Fresh surgical specimens were encased in OCT within a NIO slide holder, at a thickness of 250 μm , and imaged using SRH and TPEF imaging. Subsequent to imaging, the slide holder was gradually frozen using isopentane, the OCT was then carefully removed, and the specimen was re-embedded in a fresh OCT block. To ensure precision during the ensuing slicing procedure of the 250 μm tissue specimen, the OCT block used for re-embedding was pre-sliced to preserve the original cutting angle of the cryotome. The block, post 24 h freezing in nitrogen, was sectioned until the presence of tissue was confirmed. The initial two 10 μm sections were reserved for immunohistochemistry and immunofluorescence analyses. The third 10 μm slide was then embedded onto a Visium 10X slide, facilitating the execution of spatially resolved transcriptomic analysis.

Spatially resolved transcriptomics

Tissue fixation was performed following the 'Methanol Fixation, H&E Staining and Imaging for Visium Spatial Protocols' (CG000160, Rev C), which included heating the slide and immersing it in pre-chilled methanol. In the tissue staining phase, isopropanol was applied to tissue sections followed by a series of air-drying, haematoxylin application, washing, bluing buffer application, eosin mix addition and further washing. The slide was then dried on a heating block. Imaging was conducted using the Evos microscope, with settings following the previously described protocol (CG000160, Rev C). Permeabilization and reverse transcription were undertaken without a preceding tissue optimization on Visium tissue optimization slides, as the optimal permeabilization

time for brain tissue had been established at 12 min by a previous researcher. The overall library preparation adhered to the 'Visium Spatial Gene Expression Reagent Kits – User Guide' (CG000239, Rev F). During permeabilization, the Visium slide with stained tissue sections was fitted into a slide cassette and exposed to permeabilization enzyme, followed by a wash with 0.1X SSC buffer. For reverse transcription, an RT master mix was dispensed into each well, followed by a 45 min incubation period in a thermocycler at 53 °C. In the second-strand synthesis stage, each well received an addition of 75 μl 0.08 M KOH, followed by a brief room-temperature incubation. Subsequently, wells were washed with buffer EB and received the second-strand mix, before undergoing a 15 min incubation at 65 °C in a thermocycler. The denaturation process involved washing the wells with buffer EB and adding 35 μl 0.08 M KOH to each well, and wells were then incubated at room temperature. Afterwards, Tris (1 M pH 7.0) was pipetted into four tubes of an 8-tube strip, followed by transfer of samples from each well into these tubes. The tubes were then vortexed, centrifuged and placed on ice, with the remaining sample stored for subsequent stages. The experiment was initiated with the determination of cycle number wherein a qPCR mix was allocated across five wells of a qPCR plate, with a negative control included. The ensuing qPCR and quantification cycle (C_q) determination followed the standard protocol used for FFPE methods. Notably, uneven C_q values starting from $n.5$ were rounded up. In the subsequent complementary DNA amplification phase, an amplification mix was introduced to each sample tube, followed by thermocycling for actual PCR using a specified protocol. The cDNA cleanup process involved adding an SPRIselect reagent to each sample tube, followed by a series of incubation, washing, drying and buffer addition steps. The cleaned-up samples were then transferred to new tubes. Finally, cDNA quality control and quantification were performed using an Agilent TapeStation. The total cDNA yield was calculated, factoring in the library concentration and elution volume. The process of fragmentation, end repair and A-tailing started with using just a quarter of the purified library, with the remaining portion stored at -20 °C. The selected volume was mixed with buffer EB and fragmentation mix and incubated in a thermal cycler. Double-sided size selection was performed to discard large fragments and retain fragments within the desired size range. This involved the use of SPRIselect reagent and resulted in a library with reduced total volume and a smaller range of fragment sizes. Adaptor ligation involved mixing adaptor ligation mix with each sample and incubating in a thermocycler. Post-ligation cleanup followed the cleanup steps post-cDNA amplification, with minor adjustments to the quantities of SPRIselect reagent and buffer EB. Sample index PCR was then performed, with an amp mix and dual index TT set A added to each sample, followed by a specific PCR protocol. The total number of cycles was determined on the basis of the cDNA yield. Another round of double-sided size selection was performed, this time with varied substance quantities, to ensure another cleanup stage. The process concluded with a post-library-construction quality control, ensuring the success of the library construction. While no exact concentration calculations were necessary, the fragment size in base pairs was of interest. A fragment analyser was used due to its availability and accuracy in fragment size calculation. Sequencing was performed on a NextSeq 550 system.

Post-processing and spatially resolved transcriptomics analysis

The data analysis and quality control for this research was conducted using the 10X Genomics' space ranger pipeline and the SPATA2 (v.2.0) framework for spatial data analysis. The SPATA2 object was initiated through the 'SPATA2::initiateSpataObject_10X' function. This import procedure involved several stages using the Seurat v.4.0 package. First, gene expression normalization was performed by dividing each spot's values by the estimated total number of transcripts. These normalized values were then multiplied by 10,000 and underwent a natural logarithm transformation to improve interpretability and comparability

across genes. Next, a regression model was applied to remove batch effects and scale the data. This model factored in sample batch and the expression percentages of ribosomal and mitochondrial genes, helping to control for potential sources of unwanted variation in the data. A more detailed understanding of this process can be obtained from the guide provided at <https://themilolab.github.io/SPATA2/>. This guide provides comprehensive information about the SPATA2 package and its application in spatial transcriptomics analysis.

Post-processing and imaging analysis

The H&E images along with the PpIX and SRH images were aligned using affine transformation as described recently⁴⁴. For classification of the PpIX patterns, we extracted 160 × 160-sized patches from each barcode spot and predicted the pattern using the pretrained ResNet architecture.

Single-cell deconvolution

Cell-type deconvolution was conducted utilizing spaceX (Spatial eXpression-R): RCTD that is implemented in the SPATAWrappers package (runRCTD). This process is vital to attribute gene expression profiles to distinct cell types, improving the resolution of the spatial transcriptomics analysis. For the single-cell RNA-seq reference atlas, we made use of the recent GBMap dataset. This comprehensive dataset consists of data from over a million cells, providing a robust reference for attributing gene expression profiles to their respective cell types⁵¹.

Spatially weighted regression analysis

For spatially weighted correlation analysis, we used the function SPATAWrappers::runSpatialRegression with the following parameters: in case of multiparameter comparisons ($n > 10$), we used the model, canonical correlation analysis (CCA); for fewer parameters, we applied the Spatial Durbin linear (SLX, spatially lagged X) model or the spatial simultaneous autoregressive lag model. The parameters smooth and normalize were set as false. The spatial regression analysis provides an $n \times n$ matrix in which n refers to the selected variables with corresponding x and y positions and estimated neighbours.

Spatial cluster analysis

Spatial cluster analysis and niche definition in this study were conducted with the algorithm 'BayesSpace' specifically designed to manage the unique challenges of spatial data. Traditional clustering methods, such as k -means or shared nearest neighbour, are inadequate for spatial data because they do not take into account the physical positioning in space, an essential aspect of spatially resolved transcriptomics data. BayesSpace is a Bayesian model that clusters spatial data by considering both gene expression similarity and spatial proximity. It is an extension of the Dirichlet process mixture model, a non-parametric Bayesian approach for clustering. The BayesSpace algorithm assumes that the gene expression profile at each spot is influenced by the gene expression profiles at nearby spots. By borrowing information across spatially adjacent spots, this approach produces more robust and biologically meaningful clusters. The SPATA2 wrapper function 'SPATA2::runBayesSpaceClustering()' with default settings was used to run BayesSpace⁷³.

Gene ontology analysis

We performed differential gene expression analysis across PpIX patterns using the SPATA2 package. Differentially expressed genes were subsequently analysed by gene set enrichment analysis (GSEA) using the enrichR and GeneOverlap R packages. These packages allow the cross-referencing of an expansive collection of gene set libraries. Three gene set libraries were used in the enrichment analysis: 'GO_Biological_Process_2021', 'GO_Cellular_Component_2021' and 'GO_Molecular_Function_2021'. These libraries represent the gene ontology (GO) categories of biological process, cellular component and molecular function, respectively, up to date as of 2021.

Radiologic imaging review

Preoperative magnetic resonance imaging (MRI) scans were evaluated by a radiology resident (M.L.) with the guidance of a board-certified neuroradiologist (R.J.). Lesions were classified by enhancement pattern (homogeneous, heterogeneous, necrotic ring, nodular, non-enhancing) as commonly described in clinical practice. Lesions were evaluated for enhancement quality, enhancing margin thickness and enhancing margin definition according to the VASARI feature set (1), a validated system for describing glioma morphology on MRI. Segmentations of the enhancing tumour, non-enhancing tumour (including necrosis) and peritumoural oedema on T1-weighted pre- and post-contrast, T2-weighted and T2-FLAIR sequences were automatically generated using DeepMedic (2), a pretrained brain tumour segmentation model, and manually corrected as needed (for example, to include only the subsequently resected lesion). Segmentation volumes were calculated according to 1 mm isotropic voxels⁷⁴.

Differences in fluorescing cell densities between cases with varying CD163 density

CD163 density was assessed using a two-sided Mann–Whitney U test. A linear fixed effects model was developed to assess the impact of the time between 5-ALA administration and imaging, the proportion of enhancing tumour, the pattern of the enhancement and the Ki-67 proliferation index on the PpIX intensity measured in each case. All analyses used a significance level of 0.05 and were conducted in R.

Spatial multi-omic analysis

For spatial data analysis, we acquired the spatially resolved RNA-seq datasets using the SPATAData package (<https://github.com/theMILoLab/SPATAData>)⁴⁴. The metabolomic (MALDI) data of six patients were downloaded from <https://doi.org/10.5061/dryad.h70rx-wdmj>. We aligned the metabolomic data to the transcriptomic profiles by affine transformation of the H&E images as described recently⁴⁴. The metabolomic spectra were averaged across each transcriptomic spot with a size of 55 μm . Annotations of metabolites were performed with the Metaspace (<https://metaspace2020.eu>) database using a false discovery rate (FDR) threshold of 10%. Spatial correlation analysis was performed with either a spatial Lag model or a CCA. Cell-type deconvolution of each spot was performed by RCTD, a well-validated toolbox⁵¹. The deconvolution was performed with the SPATAWrapper (<https://github.com/heilandd-/SPATAWrappers>) package using the function runRCTD. Visualization of surface plots or correlation analysis was performed using the SPATA2 toolbox.

Spatial bulk and PpIX-sorted RNA-seq deconvolution and analysis

For analysis of the spatial bulk and PpIX-sorted cells, we used the recently published RNA-seq dataset⁵³. The data contain samples from the tumour core area (core), the contrast-enhancing rim (CE-rim) and the infiltrative regions, which were defined as weak PpIX-positive areas without defined histopathological classification, where regions are samples according to the Ivy-GAP criteria. All samples ($n = 42$) were deconvoluted to infer the cellular distribution using the pan-GBM single-cell data GBMap⁵². The full-scRNA-seq dataset was downsampled by maintaining the quantitative distributions across all cellular subtypes, defined as 'annotation level 4'. Cell-type deconvolution was performed with the MuSiC algorithm⁵⁴ using the function music_prop. Copy number alterations (CNA) were performed with the SPATA2 toolbox using the runCnvAnalysis and the add-on functions of SPATAWrapper for visualization⁵¹.

Copy number analysis

CNA analysis was performed using the CNA pipeline in the SPATA2 R tool available in the development branch, <https://github.com/theMILoLab/SPATA2>. Copy number variations (CNVs) were estimated by aligning genes to their chromosomal location and applying a moving average

to the relative expression values, with a sliding window of 100 genes within each chromosome, as described recently⁷⁵. First, genes were arranged according to their respective genomic localization using the InferCNV package (R software)⁷³. As a reference set of non-malignant cells, we used a spatial transcriptomic dataset from a non-malignant cortex sample. The exported .RDS output files were then reimported and rearranged to defined chromosomal bins. These bins were created using the SPATAwrappers function ‘Create.ref.bins()’, with the SPATA object and the size of the given bins as input. A bin size of 1 Mbp was used, resulting in 3,847 chromosomal bins with a mean coverage of 5.5 genes per bin. Rescaling and interpolation were carried out using a 10 kbp sliding window. For normalization, we used a loess regression model, built to determine the copy-number values from the InferCNV output. Interpolation and normalization were performed using the ‘SPATAwrappers::runCNV.Normalization()’ function⁴⁴.

Reporting summary

Further information on research design is available in the Nature Portfolio Reporting Summary linked to this article.

Data availability

The data supporting the results in this study are available within the paper and its Supplementary Information. They can also be viewed at <https://www.nio-net.com> by logging in with ‘PPIX’ as the institution and with ‘Guest’ as the user. In addition, the spatial transcriptomic data for this study can be accessed at <https://zenodo.org/doi/10.5281/zenodo.10909926> (ref. 76). All raw and processed image data and patient data, including the representative images provided in the paper, are available from the authors on reasonable request, subject to approval from the Institutional Review Boards of NYU Grossman School of Medicine, Medical University Vienna, Münster University Hospital, and University of Freiburg. Source data are provided with this paper.

Code availability

The code used in this study is available via GitHub at https://github.com/heilandd/Code_ALA ref. 77.

References

- Stummer, W. et al. Fluorescence-guided resection of glioblastoma multiforme by using 5-aminolevulinic acid-induced porphyrins: a prospective study in 52 consecutive patients. *J. Neurosurg.* **93**, 1003–1013 (2000).
- Widhalm, G. et al. 5-aminolevulinic acid is a promising marker for detection of anaplastic foci in diffusely infiltrating gliomas with nonsignificant contrast enhancement. *Cancer* **116**, 1545–1552 (2010).
- Stummer, W. et al. Fluorescence-guided surgery with 5-aminolevulinic acid for resection of malignant glioma: a randomised controlled multicentre phase III trial. *Lancet Oncol.* **7**, 392–401 (2006).
- Schucht, P. et al. 5-ALA complete resections go beyond MR contrast enhancement: shift corrected volumetric analysis of the extent of resection in surgery for glioblastoma. *Acta Neurochir.* **156**, 305–312 (2014).
- Della Puppa, A. et al. 5-aminolevulinic acid (5-ALA) fluorescence guided surgery of high-grade gliomas in eloquent areas assisted by functional mapping. Our experience and review of the literature. *Acta Neurochir.* **155**, 965–972 (2013).
- Schucht, P. et al. Gross total resection rates in contemporary glioblastoma surgery: results of an institutional protocol combining 5-aminolevulinic acid intraoperative fluorescence imaging and brain mapping. *Neurosurgery* **71**, 927–935 (2012).
- Díez Valle, R. et al. Surgery guided by 5-aminolevulinic fluorescence in glioblastoma: volumetric analysis of extent of resection in single-center experience. *J. Neurooncol.* **102**, 105–113 (2011).
- Stummer, W. et al. Predicting the ‘usefulness’ of 5-ALA-derived tumor fluorescence for fluorescence-guided resections in pediatric brain tumors: a European survey. *Acta Neurochir.* **156**, 2315–2324 (2014).
- Kiesel, B. et al. Systematic histopathological analysis of different 5-aminolevulinic acid-induced fluorescence levels in newly diagnosed glioblastomas. *J. Neurosurg.* **129**, 341–353 (2018).
- Lau, D. et al. A prospective Phase II clinical trial of 5-aminolevulinic acid to assess the correlation of intraoperative fluorescence intensity and degree of histologic cellularity during resection of high-grade gliomas. *J. Neurosurg.* **124**, 1300–1309 (2016).
- Panciani, P. P. et al. Fluorescence and image guided resection in high grade glioma. *Clin. Neurol. Neurosurg.* **114**, 37–41 (2012).
- Roberts, D. W. et al. Coregistered fluorescence-enhanced tumor resection of malignant glioma: relationships between δ -aminolevulinic acid-induced protoporphyrin IX fluorescence, magnetic resonance imaging enhancement, and neuropathological parameters. *Clin. Artic. J. Neurosurg.* **114**, 595–603 (2011).
- Coburger, J. et al. Tumor detection with 5-aminolevulinic acid fluorescence and Gd-DTPA-enhanced intraoperative MRI at the border of contrast-enhancing lesions: a prospective study based on histopathological assessment. *Neurosurg. Focus* **36**, E3 (2014).
- Yamada, S., Muragaki, Y., Maruyama, T., Komori, T. & Okada, Y. Role of neurochemical navigation with 5-aminolevulinic acid during intraoperative MRI-guided resection of intracranial malignant gliomas. *Clin. Neurol. Neurosurg.* **130**, 134–139 (2015).
- Panciani, P. P. et al. 5-aminolevulinic acid and neuronavigation in high-grade glioma surgery: results of a combined approach. *Neurocirugia* **23**, 23–28 (2012).
- Idoate, M. A., Díez Valle, R., Echeveste, J. & Tejada, S. Pathological characterization of the glioblastoma border as shown during surgery using 5-aminolevulinic acid-induced fluorescence. *Neuropathology* **31**, 575–582 (2011).
- Belykh, Evgenii et al. Blood-brain barrier, blood-brain tumor barrier, and fluorescence-guided neurosurgical oncology: delivering optical labels to brain tumors. *Front. Oncol.* **10**, 739 (2020).
- Stummer, W. et al. In vitro and in vivo porphyrin accumulation by C6 glioma cells after exposure to 5-aminolevulinic acid. *J. Photochem. Photobiol. B* **45**, 160–169 (1998).
- Eléouet, S. et al. Heterogeneity of delta-aminolevulinic acid-induced protoporphyrin IX fluorescence in human glioma cells and leukemic lymphocytes. *Neurol. Res.* **22**, 361–368 (2000).
- Wu, S. M., Ren, Q. G., Zhou, M. O., Peng, Q. & Chen, J. Y. Protoporphyrin IX production and its photodynamic effects on glioma cells, neuroblastoma cells and normal cerebellar granule cells in vitro with 5-aminolevulinic acid and its hexylester. *Cancer Lett.* **200**, 123–131 (2003).
- Duffner, F. et al. Specific intensity imaging for glioblastoma and neural cell cultures with 5-aminolevulinic acid-derived protoporphyrin IX. *J. Neurooncol.* **71**, 107–111 (2005).
- Valdés et al. Gadolinium- and 5-aminolevulinic acid-induced protoporphyrin IX levels in human gliomas: an ex vivo quantitative study to correlate protoporphyrin IX levels and blood-brain barrier breakdown. *J. Neuropathol. Exp. Neurol.* **71**, 806–813 (2012).
- Müther, M., Jaber, M., Johnson, T. D., Orringer, D. A. & Stummer, W. A data-driven approach to predicting 5-aminolevulinic acid-induced fluorescence and world health organization grade in newly diagnosed diffuse gliomas. *Neurosurgery* **90**, 800–806 (2022).
- Valdés, Pablo A. et al. Quantitative fluorescence in intracranial tumor: implications for ALA-induced PpIX as an intraoperative biomarker. *J. Neurosurg.* **115**, 11–17 (2011).

25. Stummer, W. et al. Intraoperative detection of malignant gliomas by 5-aminolevulinic acid-induced porphyrin fluorescence. *Neurosurgery* **42**, 518–525 (1998).
26. Hollon, T. C. et al. Near real-time intraoperative brain tumor diagnosis using stimulated Raman histology and deep neural networks. *Nat. Med.* **26**, 52–58 (2020).
27. Hollon, T. C. et al. Rapid intraoperative diagnosis of pediatric brain tumors using stimulated Raman histology. *Cancer Res.* **78**, 278–289 (2018).
28. Orringer, D. A. et al. Rapid intraoperative histology of unprocessed surgical specimens via fibre-laser-based stimulated Raman scattering microscopy. *Nat. Biomed. Eng.* **1**, 0027 (2017).
29. Hollon, T. C. et al. Rapid, label-free detection of diffuse glioma recurrence using intraoperative stimulated Raman histology and deep neural networks. *Neuro Oncol.* **23**, 144–155 (2021).
30. Freudiger, C. W. et al. Stimulated Raman scattering microscopy with a robust fibre laser source. *Nat. Photonics* **8**, 153–159 (2014).
31. Lu, H. et al. Fluorescence spectroscopy study of protoporphyrin IX in optical tissue simulating liquid phantoms. *Materials* **13**, 2105 (2020).
32. Suero Molina, E., Kaneko, S., Black, D. & Stummer, W. 5-aminolevulinic acid-induced porphyrin contents in various brain tumors: implications regarding imaging device design and their validation. *Neurosurgery* **89**, 1132–1140 (2021).
33. Leppert, J. et al. Multiphoton excitation of autofluorescence for microscopy of glioma tissue. *Neurosurgery* **58**, 759–767 (2006).
34. Bankhead, P. et al. QuPath: open source software for digital pathology image analysis. *Sci. Rep.* **7**, 16878 (2017).
35. Capper, D. et al. DNA methylation-based classification of central nervous system tumours. *Nature* **555**, 469–474 (2018).
36. Glaser, A. K. et al. Light-sheet microscopy for slide-free non-destructive pathology of large clinical specimens. *Nat. Biomed. Eng.* **1**, 0084 (2017).
37. Hambardzumyan, D., Gutmann, D. H. & Kettenmann, H. The role of microglia and macrophages in glioma maintenance and progression. *Nat. Neurosci.* **19**, 20–27 (2016).
38. Louis et al. The 2021 WHO classification of tumors of the central nervous system: a summary. *Neuro Oncol.* **23**, 8 (2021).
39. Kiesel, B. et al. 5-ALA-induced fluorescence as a marker for diagnostic tissue in stereotactic biopsies of intracranial lymphomas: experience in 41 patients. *Neurosurg. Focus* **44**, E7 (2018).
40. Wadiura, L. I. et al. High diagnostic accuracy of visible 5-ALA fluorescence in meningioma surgery according to histopathological analysis of tumor bulk and peritumoral tissue. *Lasers Surg. Med.* **53**, 300–308 (2021).
41. Millesi, M. et al. 5-ALA fluorescence for intraoperative visualization of spinal ependymal tumors and identification of unexpected residual tumor tissue: experience in 31 patients. *J. Neurosurg. Spine* **34**, 374–382 (2020).
42. Potapov, A. A. et al. Laser biospectroscopy and 5-ALA fluorescence navigation as a helpful tool in the meningioma resection. *Neurosurg. Rev.* **39**, 437–447 (2016).
43. Marbacher, S. et al. Use of fluorescence to guide resection or biopsy of primary brain tumors and brain metastases. *Neurosurg. Focus* **36**, E10 (2014).
44. Chen, T. et al. CD163, a novel therapeutic target, regulates the proliferation and stemness of glioma cells via casein kinase 2. *Oncogene* **38**, 1183–1199 (2019).
45. Ravi, V. M. et al. Spatially resolved multi-omics deciphers bidirectional tumor-host interdependence in glioblastoma. *Cancer Cell* **40**, 639–655.e13 (2022).
46. Ren, Y. et al. Spatial transcriptomics reveals niche-specific enrichment and vulnerabilities of radial glial stem-like cells in malignant gliomas. *Nat. Commun.* **14**, 1028 (2023).
47. Ravi, V. M. et al. T-cell dysfunction in the glioblastoma microenvironment is mediated by myeloid cells releasing interleukin-10. *Nat. Commun.* **13**, 925 (2022).
48. Mathewson, N. D. et al. Inhibitory CD161 receptor identified in glioma-infiltrating T cells by single-cell analysis. *Cell* **184**, 1281–1298 (2021).
49. Hara, T. et al. Interactions between cancer cells and immune cells drive transitions to mesenchymal-like states in glioblastoma. *Cancer Cell* **39**, 779–792 (2021).
50. Ito, H. et al. Oral administration of 5-aminolevulinic acid induces heme oxygenase-1 expression in peripheral blood mononuclear cells of healthy human subjects in combination with ferrous iron. *Eur. J. Pharmacol.* **833**, 25–33 (2018).
51. Pinton, L. et al. The immune suppressive microenvironment of human gliomas depends on the accumulation of bone marrow-derived macrophages in the center of the lesion. *J. Immunother. Cancer* **7**, 58 (2019).
52. Cable, D. M. et al. Robust decomposition of cell type mixtures in spatial transcriptomics. *Nat. Biotechnol.* **40**, 517–526 (2022).
53. Ruiz-Moreno, C. et al. Harmonized single-cell landscape, intercellular crosstalk and tumor architecture of glioblastoma. Preprint at *bioRxiv* <https://doi.org/10.1101/2022.08.27.505439> (2022).
54. Smith, S. J. et al. Metabolism-based isolation of invasive glioblastoma cells with specific gene signatures and tumorigenic potential. *Neuro Oncol. Adv.* **2**, vdaa087 (2020).
55. Wang, X. et al. Bulk tissue cell type deconvolution with multi-subject single-cell expression reference. *Nat. Commun.* **10**, 380 (2019).
56. Valdés, P. A. et al. Quantitative fluorescence using 5-aminolevulinic acid-induced protoporphyrin IX biomarker as a surgical adjunct in low-grade glioma surgery. *J. Neurosurg.* **123**, 771–780 (2015).
57. Valdes, P. A. et al. 5-aminolevulinic acid-induced protoporphyrin IX fluorescence in meningioma: qualitative and quantitative measurements in vivo. *Oper. Neurosurg.* **10**, 74–83 (2014).
58. Ma, R. & Watts, C. Selective 5-aminolevulinic acid-induced protoporphyrin IX fluorescence in gliomas. *Acta Neurochir.* **158**, 1935–1941 (2016).
59. Schatlo, B. et al. 5-aminolevulinic acid fluorescence indicates perilesional brain infiltration in brain metastases. *World Neurosurg. X* **5**, 100069 (2020).
60. La Rocca, G. et al. 5-aminolevulinic acid false positives in cerebral neuro-oncology: not all that is fluorescent is tumor. A case-based update and literature review. *World Neurosurg.* **137**, 187–193 (2020).
61. Marhold, F. et al. Detailed analysis of 5-aminolevulinic acid induced fluorescence in different brain metastases at two specialized neurosurgical centers: experience in 157 cases. *J. Neurosurg.* **133**, 1032–1043 (2019).
62. Liu, Y. et al. Cytoreductive surgery under aminolevulinic acid-mediated photodynamic diagnosis plus hyperthermic intraperitoneal chemotherapy in patients with peritoneal carcinomatosis from ovarian cancer and primary peritoneal carcinoma: results of a phase I trial. *Ann. Surg. Oncol.* **21**, 4256–4262 (2014).
63. Sari Motlagh, R. et al. Impact of enhanced optical techniques at time of transurethral resection of bladder tumour, with or without single immediate intravesical chemotherapy, on recurrence rate of non-muscle-invasive bladder cancer: a systematic review and network meta-analysis of randomized trials. *BJU Int.* **128**, 280–289 (2021).
64. Liu, Z. et al. Single-cell analysis of 5-ALA intraoperative labeling specificity for glioblastoma. *J. Neurosurg.* **140**, 968–978 (2023).
65. Brown, N. F., Carter, T. J., Ottaviani, D. & Mulholland, P. Harnessing the immune system in glioblastoma. *Br. J. Cancer* **119**, 1171–1181 (2018).

66. Lim, M., Xia, Y., Bettgowda, C. & Weller, M. Current state of immunotherapy for glioblastoma. *Nat. Rev. Clin. Oncol.* **15**, 422–442 (2018).
67. Ott, M., Prins, R. M. & Heimberger, A. B. The immune landscape of common CNS malignancies: implications for immunotherapy. *Nat. Rev. Clin. Oncol.* **18**, 729–744 (2021).
68. Li, H. et al. Comprehensive analysis of CD163 as a prognostic biomarker and associated with immune infiltration in glioblastoma multiforme. *BioMed. Res. Int.* **2021**, 8357585 (2021).
69. Geribaldi-Doldán, N. et al. The role of microglia in glioblastoma. *Front. Oncol.* **10**, 603495 (2020).
70. Arrieta, V. A. et al. ERK1/2 phosphorylation predicts survival following anti-PD-1 immunotherapy in recurrent glioblastoma. *Nat. Cancer* **2**, 1372–1386 (2021).
71. Vardaki, M. Z. & Kourkoumelis, N. Tissue phantoms for biomedical applications in Raman spectroscopy: a review. *Biomed. Eng. Comput. Biol.* **11**, 1179597220948100 (2020).
72. McInnes, L., Healy, J. & Melville, J. UMAP: uniform manifold approximation and projection for dimension reduction. Preprint at <https://doi.org/10.48550/arXiv.1802.03426> (2018).
73. Zhao, E. et al. Spatial transcriptomics at subspot resolution with BayesSpace. *Nat. Biotechnol.* **39**, 1375–1384 (2021).
74. Kamnitsas, K. et al. Efficient multi-scale 3D CNN with fully connected CRF for accurate brain lesion segmentation. *Med. Image Anal.* **36**, 61–78 (2017).
75. Patel, A. P. et al. Single-cell RNA-seq highlights intratumoral heterogeneity in primary glioblastoma. *Science* **344**, 1396–1401 (2014).
76. Heiland, D. H. Localization of protoporphyrin IX in glioma patients with paired stimulated Raman histology and two-photon 3 excitation fluorescence microscopy. *Zenodo* <https://doi.org/10.5281/zenodo.10909927> (2024).
77. Heiland, D. H. heilandd / Code_ALA. *GitHub* https://github.com/heilandd/Code_ALA (2024).

Acknowledgements

We thank T. Peilnsteiner, A. Lang, NYU Langone's Microscopy Laboratory (RRID: SCR_017934, and Y. Deng), NYU Langone Center for Biospecimen Research and Development (NIH/NCI 5P30CA016087-33), K12NS080223 K12 grant (T.C.H.), R01-CA226527 (D.A.O.). This project was funded by the German Cancer Consortium (DKTK), Else Kröner-Fresenius Foundation (D.H.H.), TRANSCAN (BMBF: 01KT2328) (D.H.H.), the German Research Foundation (Heisenberg Program: DFG HE 8145/6-1, Funding: HE 8145/5-1), the DKTK Partner Side Freiburg (DKTK-PI) (D.H.H.), and Joint Funding Program (HematoTrac) (D.H.H.). The work is part of the MEPHISTO project (D.H.H.), funded by BMBF (iGerman Ministry of Education and Research) (project number: 031L0260B). This research was also funded in whole or in part by the Austrian Science Fund (FWF)

(J 4725-B). Illustrations in Figs. 4a, 5a, 6a and e were created with [BioRender.com](https://www.biorender.com).

Author contributions

M.N.-M., L.I.W., M.S. and D.A.O. conceived the study, designed the experiments and wrote the article. D.J., M.M.-E., M.L., E.S.-M., W.S., R.J., D. Placantonakis, E.K.O., J.A.H., B.K., D.R., M. Mütter. and T.C.H. assisted in writing the article. M.N.-M., L.I.W., V.S., D.J., M.M.-E., E.K.L., M.L., S.H., H.W., M. Mütter, D.A., S.R., S.P., C.F., A.S., M. Mischkulnig, J.S., N.N., O.S., J.B. and D.H.H. analysed the data. M.N.-M. and D.H.H. performed statistical analyses. C.W.F. and J.T. built the SRH/TPEF microscope. D.A.O., D.H.H., G.W., W.S., D. Pacione, D. Placantonakis, K.R. and J.G.G. provided surgical specimens for imaging.

Competing interests

D.A.O. and T.C.H. are medical advisors and shareholders of Invenio Imaging, Inc., a company developing SRH microscopes. M. Mütter, W.S. and D.A.O. are consultants to NX Development Corporation, a company that markets 5-ALA for clinical use. S.R., S.P., C.W.F. and J.T. are employees and shareholders of Invenio Imaging, Inc.

Additional information

Extended data is available for this paper at <https://doi.org/10.1038/s41551-024-01217-3>.

Supplementary information The online version contains supplementary material available at <https://doi.org/10.1038/s41551-024-01217-3>.

Correspondence and requests for materials should be addressed to Dieter Henrik Heiland or Daniel A. Orringer.

Peer review information *Nature Biomedical Engineering* thanks Evgenii Belykh, Chris McKinnon, Puneet Plaha, David Roberts and the other, anonymous, reviewer(s) for their contribution to the peer review of this work.

Reprints and permissions information is available at www.nature.com/reprints.

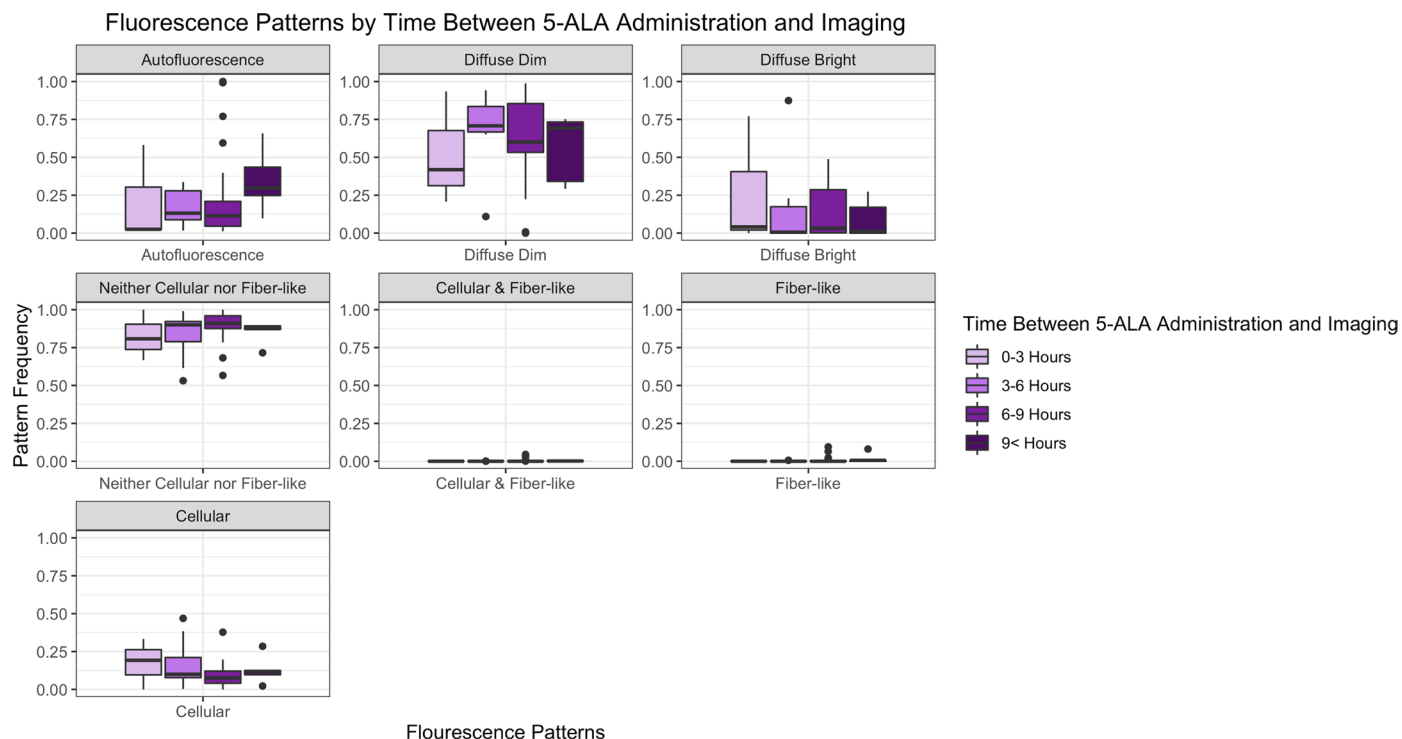
Publisher's note Springer Nature remains neutral with regard to jurisdictional claims in published maps and institutional affiliations.

Springer Nature or its licensor (e.g. a society or other partner) holds exclusive rights to this article under a publishing agreement with the author(s) or other rightsholder(s); author self-archiving of the accepted manuscript version of this article is solely governed by the terms of such publishing agreement and applicable law.

© The Author(s), under exclusive licence to Springer Nature Limited 2024

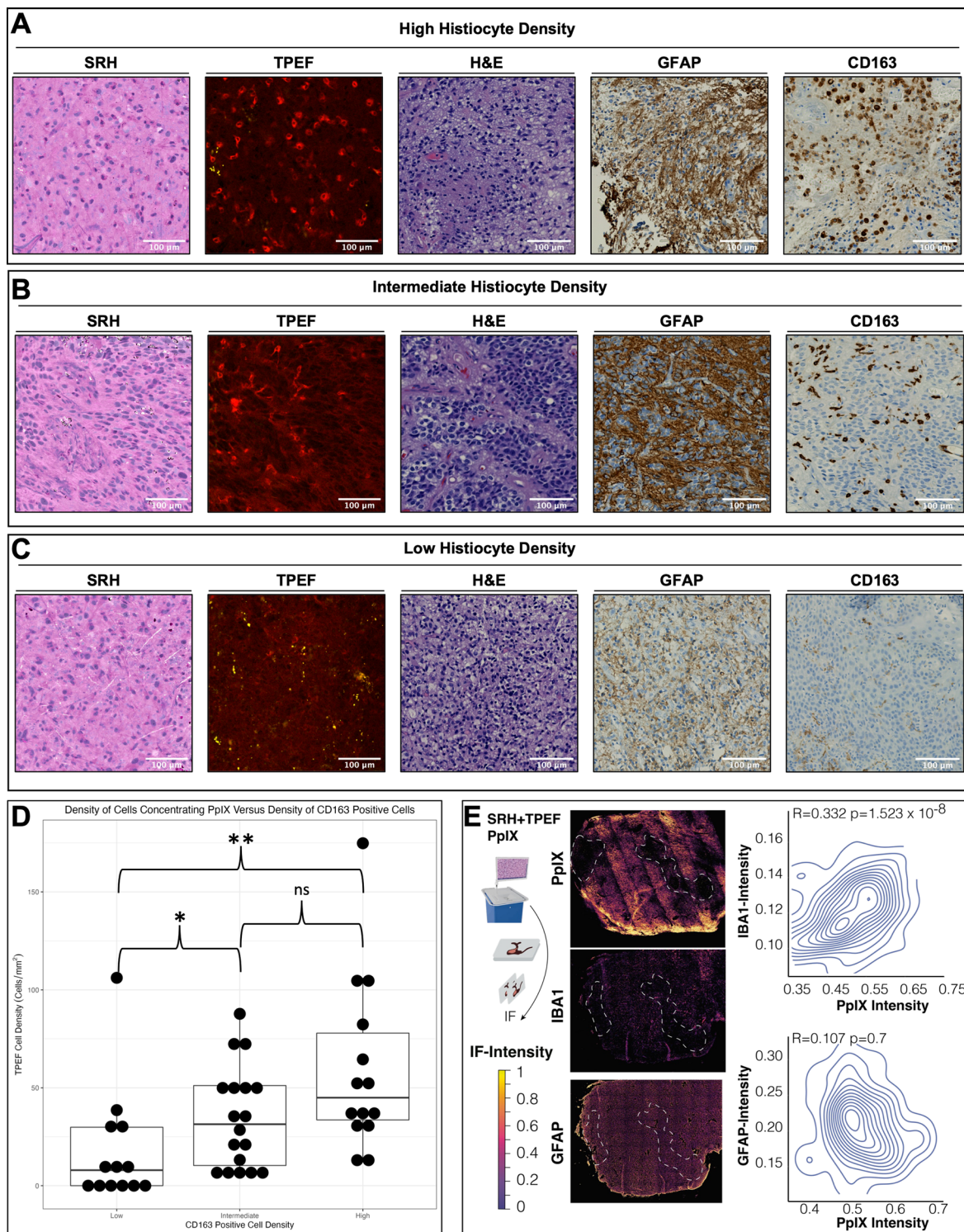
Mustafa Nasir-Moin ^{1,19}, **Lisa Irina Wadiura** ^{2,19}, **Vlad Sacalean** ^{3,4,5}, **Devin Juros** ¹, **Misha Movahed-Ezazi** ⁶, **Emily K. Lock** ¹, **Andrew Smith** ¹, **Matthew Lee** ⁷, **Hannah Weiss** ¹, **Michael Mütter** ⁸, **Daniel Alber** ¹, **Sujay Ratna** ⁹, **Camila Fang** ⁶, **Eric Suero-Molina** ⁸, **Sönke Hellwig** ⁸, **Walter Stummer** ⁸, **Karl Rössler** ², **Johannes A. Hainfellner** ¹⁰, **Georg Widhalm** ², **Barbara Kiesel** ², **David Reichert** ¹¹, **Mario Mischkulnig** ², **Rajan Jain** ⁷, **Jakob Straehle** ^{3,4,12}, **Nicolas Neidert** ^{3,4,12}, **Oliver Schnell** ^{3,4,13}, **Jürgen Beck** ^{3,4,14}, **Jay Trautman** ⁹, **Steve Pastore** ⁹, **Donato Pacione** ¹, **Dimitris Placantonakis** ¹, **Eric Karl Oermann** ^{1,15}, **John G. Golfinos** ¹, **Todd C. Hollon** ¹⁶, **Matija Snuderl** ⁶, **Christian W. Freudiger** ⁹, **Dieter Henrik Heiland** ^{3,4,5,17,18} ✉ & **Daniel A. Orringer** ^{1,6} ✉

¹Department of Neurosurgery, NYU Grossman School of Medicine, New York, NY, USA. ²Department of Neurosurgery, Medical University Vienna, Vienna, Austria. ³Department of Neurosurgery, Medical Center - University of Freiburg, Freiburg, Germany. ⁴Faculty of Medicine, University of Freiburg, Freiburg, Germany. ⁵Microenvironment and Immunology Research Laboratory, Medical Center - University of Freiburg, Freiburg, Germany. ⁶Department of Pathology, NYU Grossman School of Medicine, New York, NY, USA. ⁷Department of Radiology, NYU Grossman School of Medicine, New York, NY, USA. ⁸Department of Neurosurgery, Münster University Hospital, Münster, Germany. ⁹Invenio Imaging, Inc, Santa Clara, CA, USA. ¹⁰Division of Neuropathology and Neurochemistry (Obersteiner Institute), Department of Neurology, Medical University Vienna, Vienna, Austria. ¹¹Center for Medical Physics and Biomedical Engineering, Medical University of Vienna, Vienna, Austria. ¹²Berta-Ottenshein Clinician Scientist Program, Faculty of Medicine, University Freiburg, Freiburg, Germany. ¹³Translational NeuroOncology Research Group, Medical Center - University of Freiburg, Freiburg, Germany. ¹⁴Center for NeuroModulation (NeuroModul), University of Freiburg, Freiburg, Germany. ¹⁵Center for Data Science, New York University, New York, USA. ¹⁶Department of Neurosurgery, University of Michigan Medical School, Ann Arbor, MI, USA. ¹⁷Comprehensive Cancer Center Freiburg (CCCF), Medical Center - University of Freiburg, Freiburg, Germany. ¹⁸German Cancer Consortium (DKTK), partner site Freiburg, Freiburg, Germany. ¹⁹These authors contributed equally: Mustafa Nasir-Moin, Lisa Irina Wadiura. ✉e-mail: dieter.henrik.heiland@uniklinik-freiburg.de; Daniel.Orringer@nyulangone.org



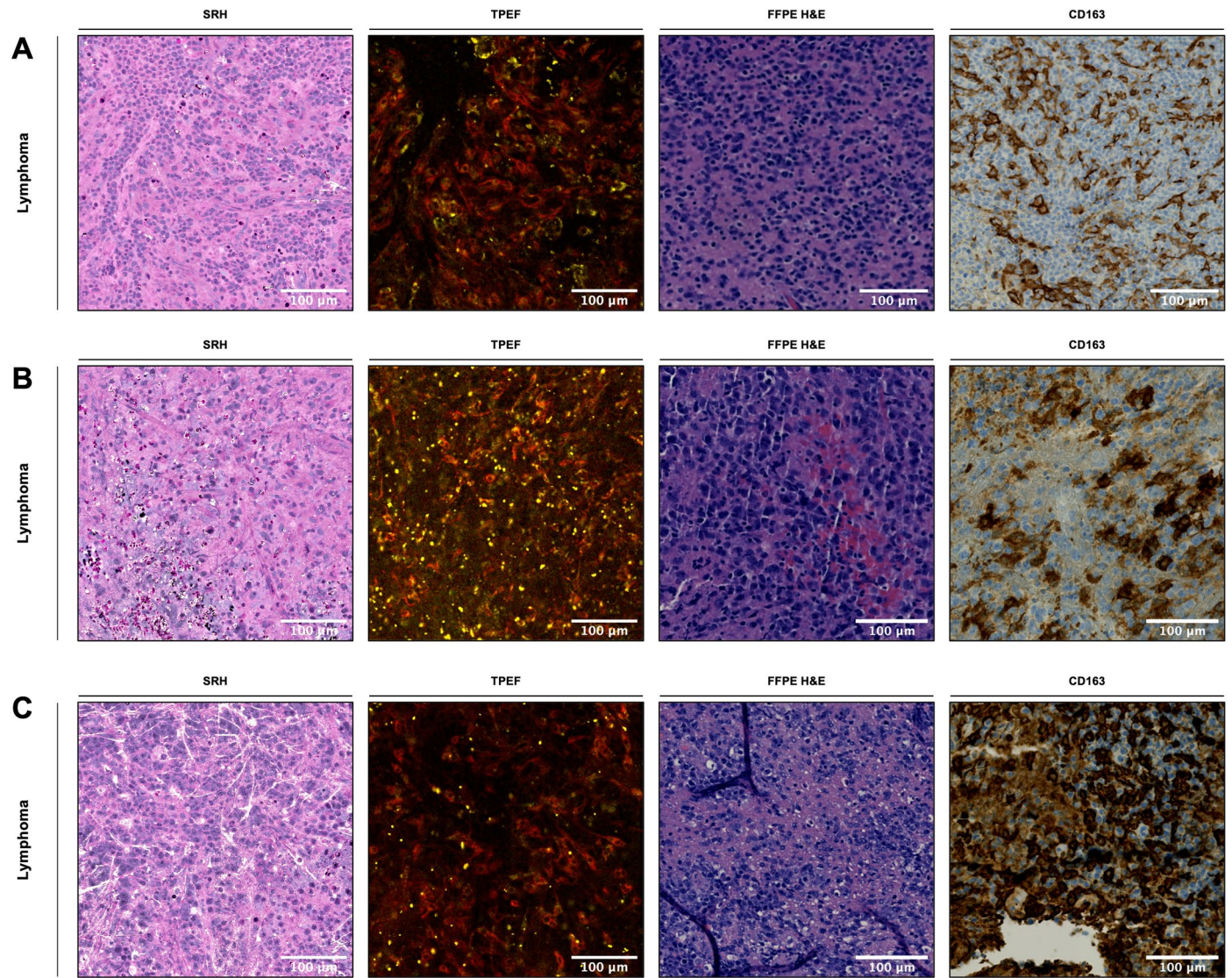
Extended Data Fig. 1 | Frequency of fluorescence patterns by time between 5-ALA administration and TPEF Imaging. The boxplots shown for each fluorescence pattern demonstrates the variation in the proportion of FOVs demonstrating the given fluorescence pattern in the given time window between

5-ALA administration and TPEF imaging. Each box ranges from the first quartile to the third quartile of the distribution and the median is marked by a line across the box. The lines extending from each box represent $\pm 1.5 \times$ interquartile range.



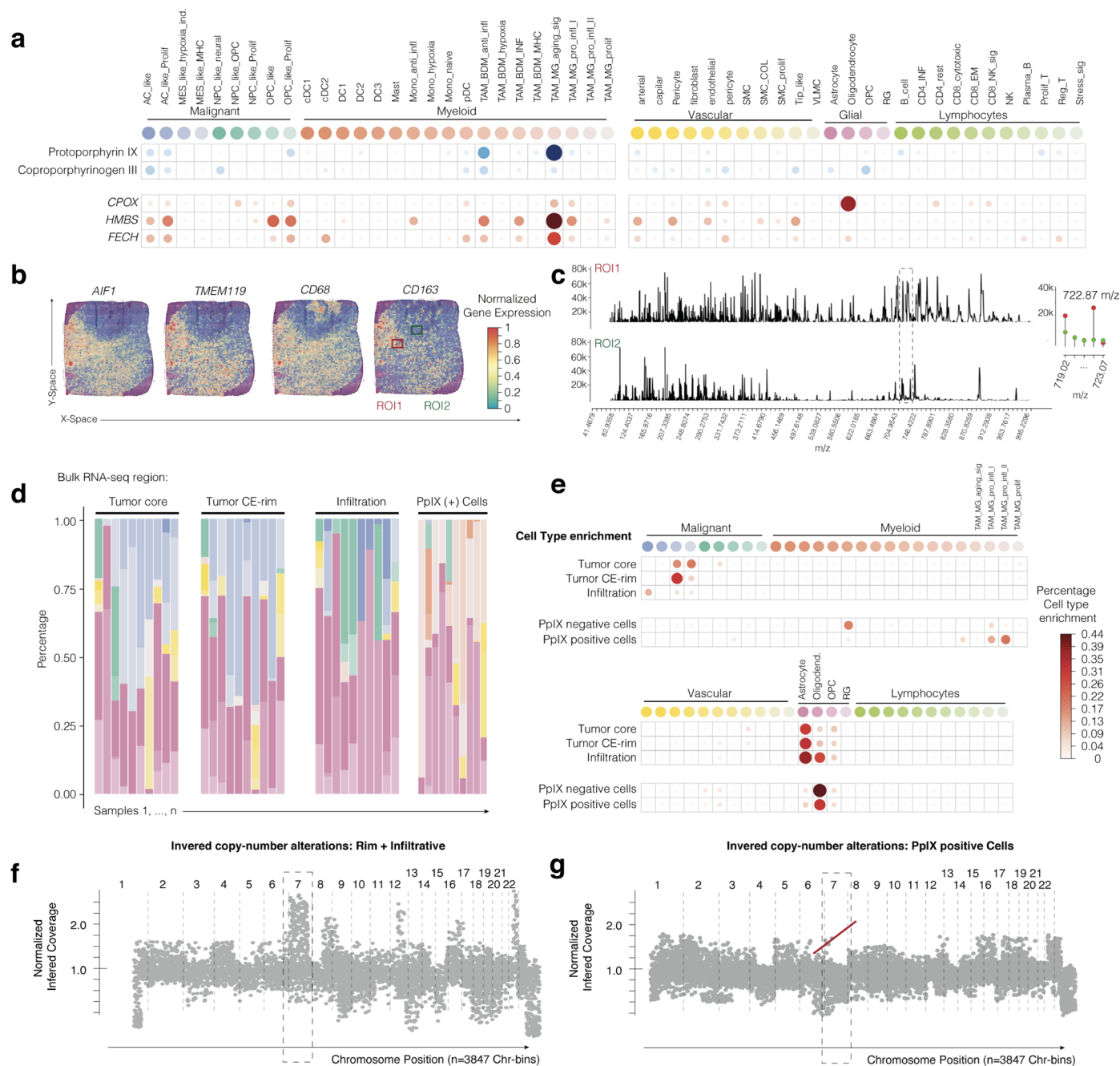
Extended Data Fig. 2 | Relationship between cellular accumulation of PpIX and abundance of histiocytes. A range of histiocyte density was encountered in the patients enrolled in our study. Specimens revealing hypercellular pleomorphic, high-grade glial neoplasms on SRH and conventional H&E reveal variations in the abundance of CD163 positive cells that correlate qualitatively with the abundance of cells with PpIX concentrated within the cytoplasm. Examples of high histiocyte density (**a**, patient 32), intermediate histiocyte density (**b**, patient 45) and low histiocyte density (**c**, patient 42) are shown here. The association of CD163 positivity and the number of cells with high PpIX cytoplasmic concentration is demonstrated in the study subjects with tissue

available for CD163 staining (**d**, $n = 45$). Cells concentrating PpIX in the cytoplasm were more abundant in specimens with intermediate (*: $p = 0.02$, two-sided Mann-Whitney U Test) and high CD163 positivity (**: $p = 0.002$, two-sided Mann-Whitney U Test) though there was no significant difference between PpIX cellularity comparing specimens with intermediate versus high CD163 positivity (n.s.: no statistical significance, $p = 0.06$, two-sided Mann-Whitney U Test). Each box ranges from the first quartile to the third quartile of the distribution and the median is marked by a line across the box. The lines extending from each box represent $\pm 1.5 \times$ interquartile range.



Extended Data Fig. 3 | CD163 staining in patients with lymphoma.
Cells accumulating PpIX in lymphoma specimens are morphologically consistent with those histiocytes present in high grade glioma specimens.

Immunohistochemistry on the same specimens revealed CD163 positive cells with similar abundance to the PpIX accumulating cells in each of the three patients (a, patient 76; b, patient 77; c, Patient 78).



Extended Data Fig. 4 | Additional transcriptomic and metabolomic analysis of PpIX accumulating cells. The spatially weighted correlation analysis of enzymes (red) and metabolites (blue) with cell type likelihood scores in six patients is displayed in the dot plot (a). The surface plot of myeloid gene expression is shown in (b). Mass spectra of selected ROIs (left) with high

resolution of the PpIX peak at 722.6 m/z are shown in (c). The cell composition of the bulk RNA-sequencing data is shown in the stacked bar graph (d). The percentage of cell type enrichment is shown in (e). The derived copy number profiles using SPATA2 toolbox for infiltrative tumor are shown in (f) and that for PpIX positive cells are shown in (g).

Reporting Summary

Nature Portfolio wishes to improve the reproducibility of the work that we publish. This form provides structure for consistency and transparency in reporting. For further information on Nature Portfolio policies, see our [Editorial Policies](#) and the [Editorial Policy Checklist](#).

Statistics

For all statistical analyses, confirm that the following items are present in the figure legend, table legend, main text, or Methods section.

n/a Confirmed

- | | | |
|-------------------------------------|-------------------------------------|--|
| <input type="checkbox"/> | <input checked="" type="checkbox"/> | The exact sample size (n) for each experimental group/condition, given as a discrete number and unit of measurement |
| <input type="checkbox"/> | <input checked="" type="checkbox"/> | A statement on whether measurements were taken from distinct samples or whether the same sample was measured repeatedly |
| <input type="checkbox"/> | <input checked="" type="checkbox"/> | The statistical test(s) used AND whether they are one- or two-sided
<i>Only common tests should be described solely by name; describe more complex techniques in the Methods section.</i> |
| <input type="checkbox"/> | <input checked="" type="checkbox"/> | A description of all covariates tested |
| <input type="checkbox"/> | <input checked="" type="checkbox"/> | A description of any assumptions or corrections, such as tests of normality and adjustment for multiple comparisons |
| <input type="checkbox"/> | <input checked="" type="checkbox"/> | A full description of the statistical parameters including central tendency (e.g. means) or other basic estimates (e.g. regression coefficient) AND variation (e.g. standard deviation) or associated estimates of uncertainty (e.g. confidence intervals) |
| <input type="checkbox"/> | <input checked="" type="checkbox"/> | For null hypothesis testing, the test statistic (e.g. F , t , r) with confidence intervals, effect sizes, degrees of freedom and P value noted
<i>Give P values as exact values whenever suitable.</i> |
| <input checked="" type="checkbox"/> | <input type="checkbox"/> | For Bayesian analysis, information on the choice of priors and Markov chain Monte Carlo settings |
| <input type="checkbox"/> | <input checked="" type="checkbox"/> | For hierarchical and complex designs, identification of the appropriate level for tests and full reporting of outcomes |
| <input type="checkbox"/> | <input checked="" type="checkbox"/> | Estimates of effect sizes (e.g. Cohen's d , Pearson's r), indicating how they were calculated |

Our web collection on [statistics for biologists](#) contains articles on many of the points above.

Software and code

Policy information about [availability of computer code](#)

Data collection Proprietary software was used in the NIO imaging system (Invenio Imaging Inc.)

Data analysis Python 3.9.0, pydicom, scikit-image 0.18.3, pandas 1.3.5, Fiji/ImageJ 2.1.0, R 4.1.0, tidyverse 1.3.1, ggplot2 3.3.5, ggpubr 0.4.0, tidyr 1.1.3, QuPath 0.2.3, Ranger, SPATA2 2.0, Seurat 4.0, spacexr (SPATA2 wrapper), BayesSpace (SPATA2 wrapper), enrichR, GeneOverlap, SPATADData, SPATAWrapper, inferCNV.

For manuscripts utilizing custom algorithms or software that are central to the research but not yet described in published literature, software must be made available to editors and reviewers. We strongly encourage code deposition in a community repository (e.g. GitHub). See the Nature Portfolio [guidelines for submitting code & software](#) for further information.

Data

Policy information about [availability of data](#)

All manuscripts must include a [data availability statement](#). This statement should provide the following information, where applicable:

- Accession codes, unique identifiers, or web links for publicly available datasets
- A description of any restrictions on data availability
- For clinical datasets or third party data, please ensure that the statement adheres to our [policy](#)

The data supporting the results in this study are available within the paper and its Supplementary Information. They can also be viewed at <https://www.nio-net.com> by logging in with "PPIX" as the institution and with "Guest" as the user. Additionally, the spatial transcriptomic data for this study can be accessed at <https://zenodo.org/doi/10.5281/zenodo.10909926>. All of the raw and processed image data and patient data, including the representative images provided in the paper,

Field-specific reporting

Please select the one below that is the best fit for your research. If you are not sure, read the appropriate sections before making your selection.

Life sciences Behavioural & social sciences Ecological, evolutionary & environmental sciences

For a reference copy of the document with all sections, see [nature.com/documents/nr-reporting-summary-flat.pdf](https://www.nature.com/documents/nr-reporting-summary-flat.pdf)

Life sciences study design

All studies must disclose on these points even when the disclosure is negative.

Sample size	The sample size was estimated at 70 patients to ensure adequate representation of all major tumour types for analysis, and was also based on the design of previous studies comparing SRS and H&E.
Data exclusions	No data were excluded other than those patients that met the exclusion criteria. Exclusion criteria: 1) Poor quality of the specimen on visual gross examination due to excessive blood, coagulation artifact, necrosis or ultrasonic damage. 2) Surgeon declares that all collected specimens must be allocated for clinical purposes. 3) Final histopathologic diagnosis is not a high-grade glioma or lymphoma, including glioblastoma, astrocytoma, anaplastic oligodendroglioma, high-grade glioma, anaplastic astrocytoma, and anaplastic neuroepithelial tumour. 4) Any unanticipated malfunction of the SRH/TPEF imaging system at the time of surgery.
Replication	Results were replicated across multiple health centers with multiple SRH/TPEF imaging systems.
Randomization	Randomization was not applicable to the study.
Blinding	Blinding was not applicable to the study.

Reporting for specific materials, systems and methods

We require information from authors about some types of materials, experimental systems and methods used in many studies. Here, indicate whether each material, system or method listed is relevant to your study. If you are not sure if a list item applies to your research, read the appropriate section before selecting a response.

Materials & experimental systems

n/a	Included in the study
<input type="checkbox"/>	<input checked="" type="checkbox"/> Antibodies
<input checked="" type="checkbox"/>	<input type="checkbox"/> Eukaryotic cell lines
<input checked="" type="checkbox"/>	<input type="checkbox"/> Palaeontology and archaeology
<input checked="" type="checkbox"/>	<input type="checkbox"/> Animals and other organisms
<input type="checkbox"/>	<input checked="" type="checkbox"/> Human research participants
<input type="checkbox"/>	<input checked="" type="checkbox"/> Clinical data
<input checked="" type="checkbox"/>	<input type="checkbox"/> Dual use research of concern

Methods

n/a	Included in the study
<input checked="" type="checkbox"/>	<input type="checkbox"/> ChIP-seq
<input checked="" type="checkbox"/>	<input type="checkbox"/> Flow cytometry
<input checked="" type="checkbox"/>	<input type="checkbox"/> MRI-based neuroimaging

Antibodies

Antibodies used	Roche Diagnostics, Cat #760-4437, MRQ-26 Mouse Monoclonal Antibody
Validation	Immunohistochemistry using clinically validated antibodies for CD163, and performed in a CLIA certified laboratory.

Human research participants

Policy information about [studies involving human research participants](#)

Population characteristics	Inclusion criteria for the intraoperative SRH/TPEF imaging included: 1) Male or female of any age. 2) Patients undergoing central nervous system tumour resection at NYU Langone Medical Center, Medical University Vienna, Münster University Hospital, or University of Freiburg.
Recruitment	All patients with newly diagnosed or recurrent brain lesions/suspected brain tumors were approached for recruitment. Recruitment occurred in both the outpatient and inpatient settings. Patients were informed that the study was to assess a

non-interventional imaging modality only. Patients were further informed that no additional tissue would be collected beyond that need for clinical diagnosis except when they provided their informed consent.

Ethics oversight

Complete Institutional Review Board oversight.

Note that full information on the approval of the study protocol must also be provided in the manuscript.

Clinical data

Policy information about [clinical studies](#)

All manuscripts should comply with the ICMJE [guidelines for publication of clinical research](#) and a completed [CONSORT checklist](#) must be included with all submissions.

Clinical trial registration

Not applicable. This study was a non-interventional imaging study conducted at NYU Langone Medical Center, Medical University Vienna, Münster University Hospital, and University of Freiburg.

Study protocol

Full study protocol can be obtained from the corresponding author on request.

Data collection

The study was conducted at NYU Langone Medical Center, Medical University Vienna, Münster University Hospital, University of Freiburg. Prospective enrollment began on November 2, 2020 and closed on March 1, 2023.

Outcomes

The primary outcome measure was the validation of the SRH/TPEF imaging system. The secondary outcome was the correlation between tumour cell density and protoporphyrin IX fluorescence. The third outcome was the characterization of protoporphyrin IX fluorescence patterns with spatial transcriptomics.